Tulips R
University of Tsukuba
Repository

Annual Report April 1, 2011 - March 31, 2012

journal or publication title	University of Tsukuba Tandem Accelerator Complex (UTTAC) Annual Report
number	2011
year	2012
URL	http://hdl.handle.net/2241/00145854

UTTAC-81, 2012

UTTAC

ANNUAL REPORT 2011

TANDEM ACCELERATOR COMPLEX
Research Facility Center for Science and Technology
University of Tsukuba

http://www.tac.tsukuba.ac.jp/

UTTAC

ANNUAL REPORT 2011

April 1, 2011 – March 31, 2012

UTTAC-81, 2012

Executive Editor: Eiji Kita
Editors: Yoshihiro Yamato, Daiichiro Sekiba, Kimikazu Sasa, and Tetsuro Komatsubara

---

UTTAC is a series of issues, which include annual reports of
Tandem Accelerator Complex, Research Facility Center
for Science and Technology, University of Tsukuba.
The issues may also include irregular reports written by English.

Copyright © 2012 by Tandem Accelerator Complex, Research Facility Center
for Science and Technology, University of Tsukuba and individual contributors.

All reports are written on authors' responsibility and thus the editors are not liable
for the contents of the report.

Tandem Accelerator Complex, Research Facility Center for Science and Technology,
University of Tsukuba
Tennodai 1-1-1, Tsukuba, Ibaraki 305-8577, Japan

http://www.tac.tsukuba.ac.jp/
annual@tac.tsukuba.ac.jp

PREFACE

This annual report covers researches carried out at Tandem Accelerator Complex, Research Facility Center for Science and Technology, the University of Tsukuba (UTTAC), during the fiscal year 2011 (April 1st 2011 ~ March 31st 2012). Since the 12UD Pelletron tandem accelerator has been completely destroyed by the Great East Japan Earthquake on March 11th 2011, contents of this volume are limited to the researches by use of the 1 MV Tandetron accelerator and ^{57}Co Mössbauer spectroscopy. Then, the number of pages of this volume becomes a little fewer than those of the older volumes.

The government has been supporting repairs and maintenances for damaged buildings and facilities, and our 12UD accelerator was also covered by the reconstruction budget through the Ministry of Education, Culture, Sports, Science and Technology Japan (MEXT). The damage of the 12UD accelerator was, however, too serious and severe to repair. Therefore, we gave it up and decided to replace by a new 6 MV tandem accelerator. It is now under construction by NEC (National Electrostatics Corporation, at Middleton, Wisconsin, USA). The expecting date arriving at Tsukuba will be around the spring of 2014. We are looking forward to operating the new 6 MV accelerator and reporting about it.

December 1st 2012

Editors

CONTENTS

1. ACCELERATOR AND EXPERIMENTAL FACILITIES

1.1 Accelerator operation (2011). ····· 1

1.2 Post-quake reconstruction project of the Tandem Accelerator Facility at the University of Tsukuba ····· 3

1.3 Development of rotating magnetic field applying system for β-NMR method ····· 5

2. NUCLEAR PHYSICS

2.1 Measurement of the astrophysical S-factor for the reaction $^{7}Li(^{3}He, p)^{9}Be$ at 3MeV····· 7

2.2 The study of nucleosyntesis by means of scandium-45 + p reaction····· 9

3. MATERIAL AND CLUSTER SCIENCE

3.1 Hydrogen uptake process in a-C:H film growth studied by RBS-ERDA with hydrogen isotope ····· 11

3.2 Droplet formation in $N_2/H_2O/SO_2$ by corona discharge ····· 12

3.3 Measurement of secondary electron yields with a micro-channel plate or the study of cluster effects ····· 14

3.4 Investigation of layer thicknesses in CaF_2/Fe_3Si heterostructures grown on Si(111) substrates by molecular beam epitaxy ····· 16

3.5 Conversion electron Mössbauer spectroscopy (CEMS) study of an iron oxide thin film fabricated by reactive sputtering ····· 18

3.6 Mössbauer analysis of Mg-containing Fe_3O_4 nanoparticles for magnetic hyperthermia ····· 20

4. INTERDISCIPLINARY RESEARCH

4.1 Direct characterization of hydrogen content in MLCC employing elastic recoil coincidence spectroscopy ····· 23

5. LIST OF PUBLICATIONS

5.1 Journals ····· 27

5.2 International conferences ····· 32

6. THESES 34

7. SEMINARS 36

8. SYMPOSIUM 37

9. LIST OF PERSONEL 39

1.

ACCELERATOR AND EXPERIMENTAL FACILITIES

1.1 Accelerator operation 2011

K. Sasa, S. Ishii, H. Kimura, H. Oshima, Y. Tajima, T. Takahashi, Y. Yamato,
T. Komatsubara, D. Sekiba and E. Kita.

The 12UD Pelletron tandem and the 1 MV Tandetron accelerators have been operated and maintained at the University of Tsukuba, Tandem Accelerator Complex (UTTAC). However, the 12UD Pelletron tandem accelerator suffered serious damage from the Great East Japan Earthquake on 11 March 2011. We decided to shut down the 12UD Pelletron tandem accelerator on January 2012. The 1 MV Tandetron accelerator did not have any serious damage, therefore we used only the 1 MV Tandetron accelerator for experimental researches in 2011.

The total service time of the UTTAC multi-tandem accelerator facility was 1,968 hours in the fiscal year 2011. 34.9 percent (686 hours) of the total service time were used for industrial users under the project "Promotion of Advanced R&D Facility Utilization", which was supported financially by the Ministry of Education, Culture, Sports, Science and Technology (MEXT) of JAPAN. In the project, a total of 11 research programs were conducted in 2011.

The 1 MV Tandetron accelerator

The operating time and the experimental beam time of the 1 MV Tandetron accelerator were 826.5 and 380.6 hours, respectively, during the total service time in 2011. A total of 68 research programs were carried out and a total of 677 researchers used the 1 MV Tandetron accelerator. Fig. 1 shows the percentage of accelerated ions for the 1 MV Tandetron accelerator. Fig. 2 shows the percentage of the experimental beam time for the running research fields.

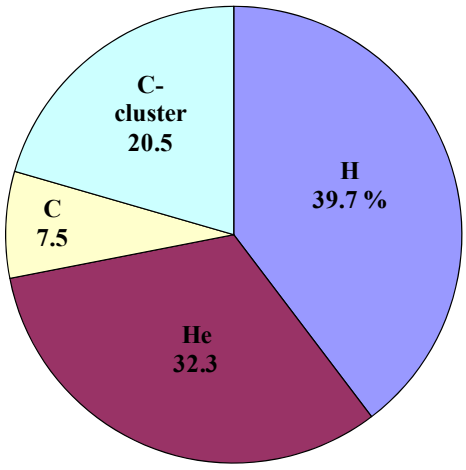

Fig.1. Percentage of accelerated ions for the 1 MV Tandetron accelerator in 2011.

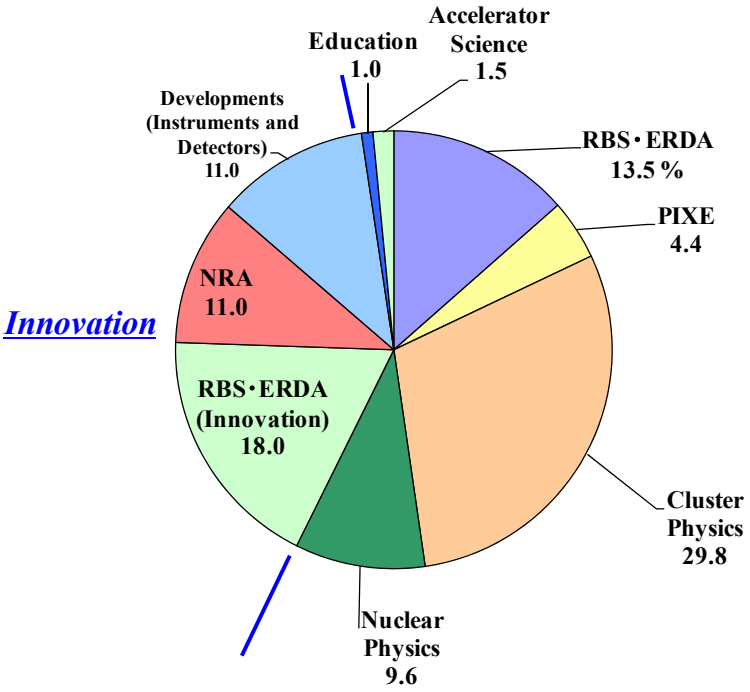

Fig.2. Percentage of the experimental beam time for the running research fields with the 1 MV Tandetron accelerator in 2011.

1.2 Post-quake reconstruction project of the Tandem Accelerator Facility at the University of Tsukuba

K. Sasa, S. Ishii, H. Kimura, H. Oshima, Y. Tajima, T. Takahashi, Y. Yamato,
T. Komatsubara, D. Sekiba and E. Kita.

We are planning to install a new middle-sized tandem accelerator at the 2nd experimental room instead of the broken 12UD Pelletron tandem accelerator. The renewed tandem accelerator system will widely be applied for AMS, IBA, beam irradiation research and nuclear physics.

In 2011, we repaired damaged experimental rooms and leaky roofs by the earthquake. Fig. 1 shows a photo of the 2nd experimental room under repair. After restoration, we removed all beam lines in the 2nd experimental room in order to construct the renewed tandem accelerator system. Fig. 2 shows the current state of the 2nd experimental room.

Fig. 1. A photo of the 2nd experimental room under repair.

Fig. 2. Current state of the 2nd experimental room after removal of all beam lines.

The renewed tandem accelerator system will consist of a horizontal type 6 MV Pelletron tandem accelerator, new 4 ion sources and the polarized ion source, an accelerator mass spectrometry system and an ion beam analysis system. The 6 MV Pelletron tandem accelerator is designed by the National Electrostatics Corp., USA. Fig. 3 shows the schematic view of the 6 MV Pelletron tandem accelerator. The accelerator tank is about 8.8 m long and 2.7 m in diameter.

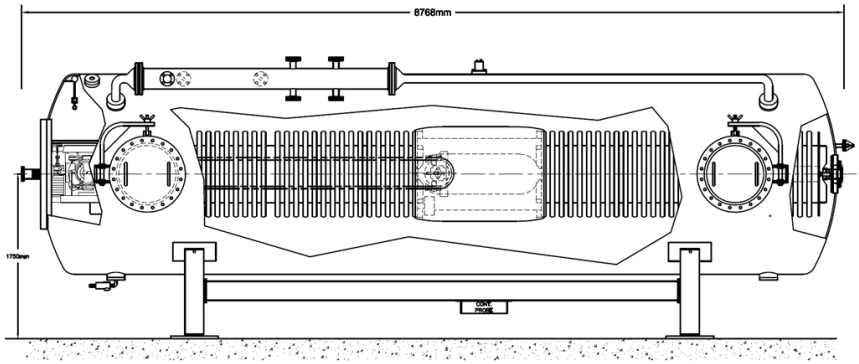

Fig. 3. Schematic view of the 6 MV Pelletron tandem accelerator designed by the National Electrostatic Corp., USA.

The polarized ion source was damaged in the earthquake. After restoration of the polarized ion source, it will be moved from the 9th floor to a new experimental booth at the ground. A high energy beam transport line will be connected from the new tandem accelerator to the present experimental facilities in the 1st experimental room. The beam transport line will intersect with another beam line for AMS and IBA in the 2nd experimental room. Fig. 4 shows the layout of the new 6 MV tandem accelerator system. The AMS system will be capable of measuring environmental levels of long-lived radioisotopes of ^{10}Be, ^{14}C, ^{26}Al, ^{36}Cl, ^{41}Ca and ^{129}I. The IBA system will be equipped with a high-precision five-axis goniometer. The construction of the new 6 MV tandem accelerator system is scheduled in the spring of 2014. The beam delivery will start on September 2014.

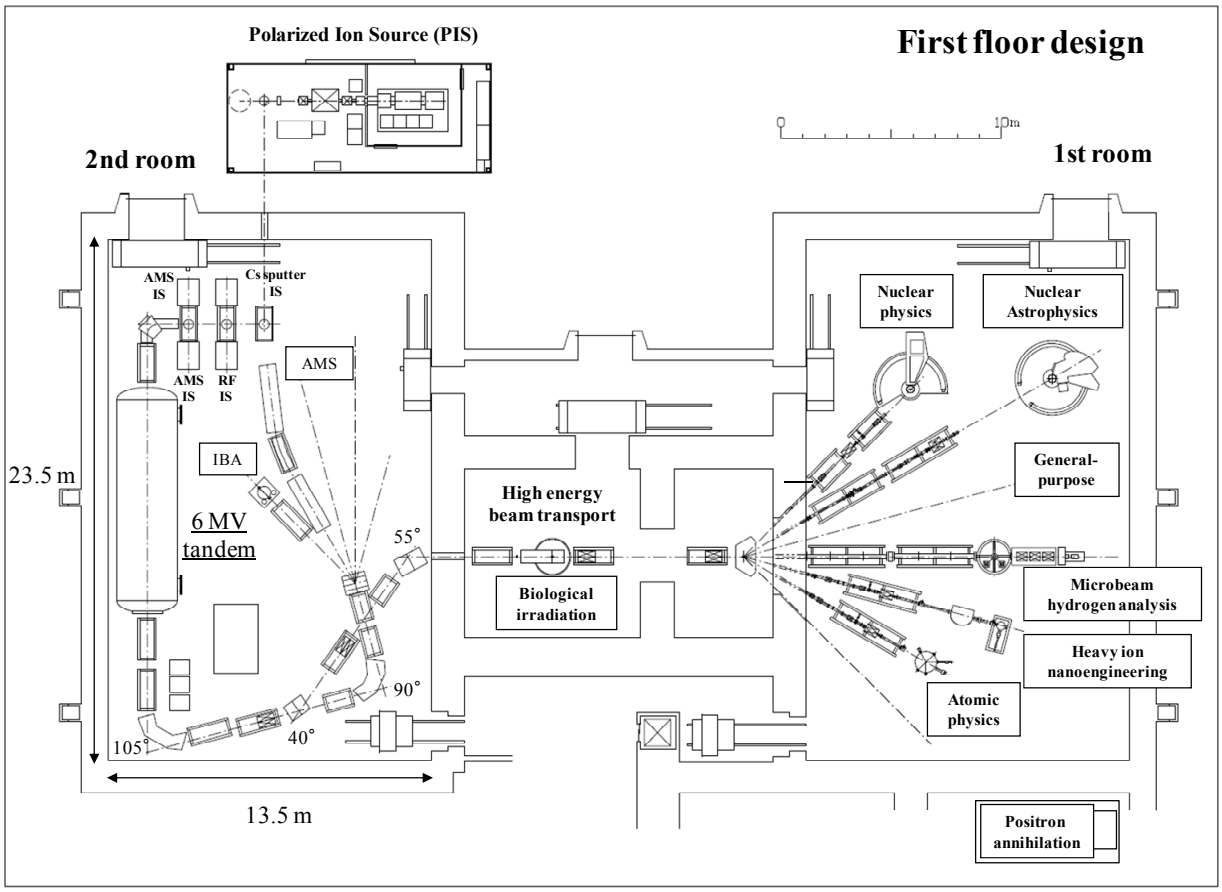

Fig.4. Layout of the new 6 MV tandem accelerator system.

1.3 Development of rotating magnetic field applying system for β-NMR method

T. Niwa, D. Nagae, Y. Abe, Y. Ishibashi, and A. Ozawa

The spin parity as well as the sign of magnetic (μ) moment are basic probes to obtain information about the nuclear structure throughout the entire nuclear chart. To determine a spin parity and a sign of μ moment, a laser spectroscopy[1] and decay spectroscopy[2] are mostly used. However, these measurements are limited to the specific nuclei due to some experimental restrictions especially nuclei located far from β stability region. For this region, the β-ray detected nuclear magnetic resonance (β-NMR) technique is a powerful method measuring an absolute μ moment[3, 4]. In order to determine the sign of μ moment, a β-NMR technique using rotating magnetic field is developing.

In the β-NMR technique, the μ moment is deduced from a frequency of the NMR. The NMR is measured by a detection of the NMR effect which arises in the asymmetric angular distribution of β-ray emission from spin-polarized radioactive nucleus. The resonance frequency ν under a only static magnetic field B_0 is given by $\nu = g\mu_N B_0/h$, where g, μ_N, and h denote a g factor, the nuclear magneton, and the Planck's constant, respectively. The μ moment $\mu = g\mu_N I$ is determined from the measured values ν and B_0 and spin I which is a spin of the magnetic sublevel. In a rotating coordinate system with a rotation angular frequency $\vec{\omega}$, the equation of motion for the μ moment is expressed using $\gamma = g\mu_N/h$ as

$$\frac{\partial \vec{\mu}}{\partial t} = \gamma\vec{\mu} \times \left(\vec{B}_0 + \frac{\vec{\omega}}{\gamma}\right) = \gamma\vec{\mu} \times \vec{B}_{\text{eff}}. \tag{1}$$

When we choose the rotation frequency $\vec{\omega} = -\gamma\vec{B}_0 = \vec{\omega}_0$ so that $\vec{B}_{\text{eff}} \equiv \vec{B}_0 + \vec{\omega}/\gamma = 0$, we obtain $\partial\vec{\mu}/\partial t = 0$. This result shows that $\vec{\mu}$ is precessing around $\vec{B}_0$ with an angular velocity $\vec{\omega} = \vec{\omega}_0$. Let us suppose that a rotating magnetic field $\vec{B}_1$ which is perpendicular to the static magnetic field is applied to the nucleus. When the frequency of the field is corresponds to the resonance one for the nucleus, the direction of its spin polarization is changed by the NMR. Usually, an oscillating magnetic field can be created as a superposition of right- and left-rotating magnetic fields. When one of these two components matches the resonant frequency $\vec{\omega} \approx \vec{\omega}_0$, the other component should rotate with frequency $\approx -2\vec{\omega}_0$. Since the latter component produces only a negligible effect on the motion of spin because of the high apparent frequency $2\vec{\omega}_0$, we can just neglect it. Since the applied magnetic fields are oscillating, we canft determine which component matches the resonance condition. Thus, only the absolute μ moment can be deduced by this method. In order to determine the sign of the μ moment, applying rotating magnetic field is needed.

In order to apply the rotating magnetic field, we have developed a new RF application system as shown in Fig. 1. The rotating magnetic field is obtained using two pairs of coils. The radius of coil and the distance between a pair of coils are 20 mm and 24 mm, respectively. The phase-angle difference of the alternating currents for both pairs of coins is 90 degree. Thus a composed magnetic field is circular polarized. By changing the phase-angle difference, a right- or left-circularly polarized magnetic field can be produced. A waveform appropriate for the rotating magnetic field was generated by a Function Generator (F. G.). The signal from the F.G. was split into two. One of them was fed to a pair of coils through an attenuator and a 300-W RF power amplifier. Another signal was fed into a phase shifter where

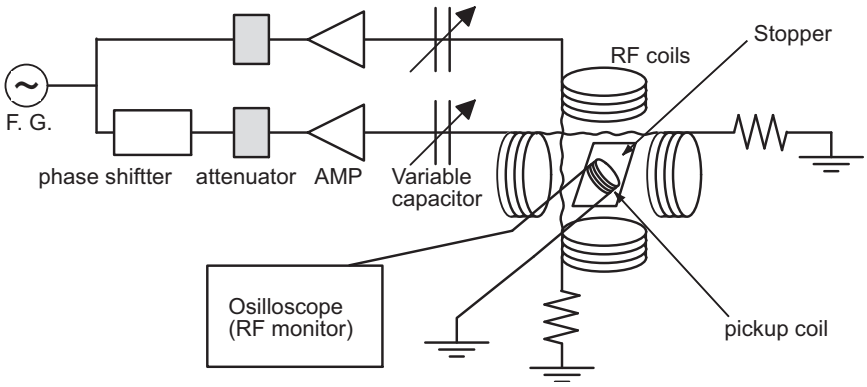

Fig. 1. Block diagram of the RF system for rotating magnetic field.

the phase angle was shifted by 90 degree. This signal was fed into another pair of coils via an attenuator and a 300-W RF power amplifier.

In order to confirm the production of the rotating magnetic field, a pickup coil is used. The pickup coil oriented by 45 degree with respect to the pairs of coils was located at the stopper position as shown in Fig. 1. Figure 2 shows a current without the phase shifter, a current with the phase shifter, and an output of pickup coil. A production of a rotating magnetic field including a liner component was confirmed by the output of pickup coil. Further efforts to measure a polarization of the rotating magnetic field are now in progress.

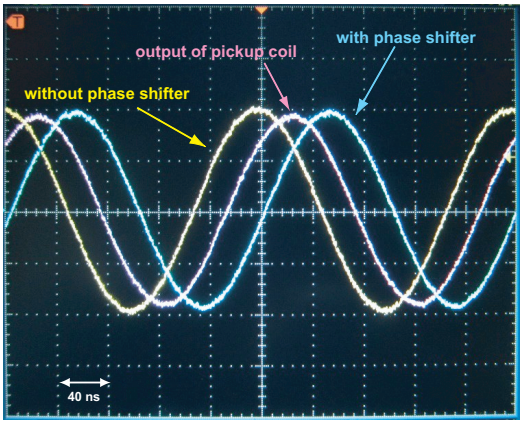

Fig. 2. A typical output of pickup coil with current with/without the phase shifter.

References

[1] G. Huber et al., Phys. Rev., **C18**, 2342(1978).

[2] D.T. Yordanov et al., Phys. Rev. Lett. **99** 212501(2007).

[3] K. Sugimoto et al., J. Phys. Soc. Jpn. **21**, 213(1966)

[4] H. Ueno et al., Phys. Lett., **B615**, 186(2005).

2.

NUCLEAR PHYSICS

2.1 Measurement of the astrophysical S-factor for the reaction ^{7}Li(^{3}He,p)^{9}Be at 3MeV.

T. Yuasa, T. Komatsubara, T. Oonishi, K. Sasa, S .Kubono[1], T. Hayakawa[2], and T. Shizuma[2]

The observations [1] of metal-poor halo stars indicate that the primordial abundances of ^{7}Li may not be in agreement with the prediction of standard big bang nucleosynthesis (BBN), where the prediction should be consistent to the baryon-to-photon ratio inferred from analysis of the Wilkinson Microwave Anisotropy Probe (WMAP) power spectrum. It suggests that the predicted vale of the abundance of ^{7}Li is about 3 times higher than the observed value [2]. The ^{7}Li yield is determined from a balance between production and destruction reactions. An accurate knowledge of both type of reactions is necessary for cosmological model calculations to be reliable. Previously, the astrophysical S-factor for the reaction ^{7}Li(^{3}He, p)^{9}Be was measured in low energy region [3-6]. But there is a missing region where no data were reported, so we have started the study to measure the astrophysical S-factor in this region.

First we have no experience to accelerate ^{3}He ions with the 1 MV Tandetron, we carried out test experiment using the ions. Although it was the first time to accelerate ^{3}He beam, we got stable and high current beam. During the test, we measured the reaction ^{7}Li(^{3}He,p)^{9}Be at 3 MeV. The target was made by evaporating lithium carbonate on a carbon film of 20 μg/cm^{2}. Reaction products were detected with a

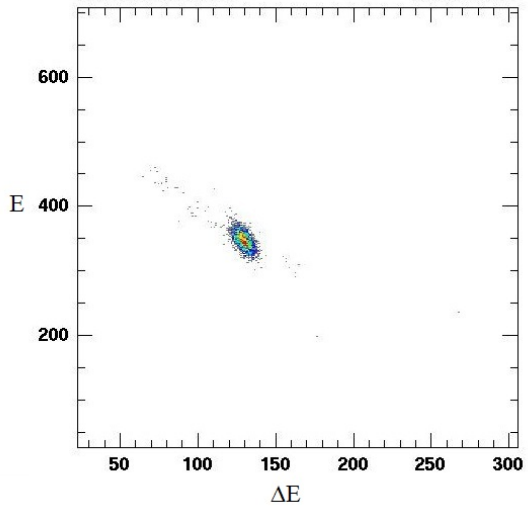

Fig 1. Contour-map of E-ΔE counter telescope for a carbon target. Protons from ^{12}C(^{3}He, p)^{14}N reaction can be observed..

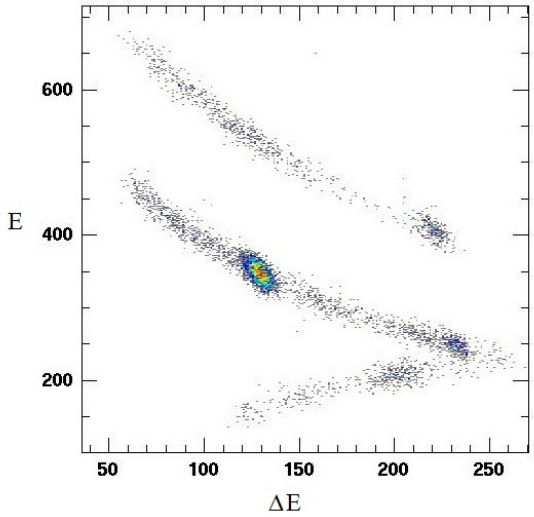

Fig 2. Contour-map of the same counter for a natural lithium carbonate target with carbon backing. Protons and deuterons can be seen.

[1] Center for Nuclear Study, Univ. of Tokyo (CNS)

[2] Japan Atomic Energy Agency (JAEA)

standard two-detector telescope of silicon surface barrier detectors. The front ΔE detector had a thickness of 150μm and the back E detector had a thickness of 500μm. We made a two-dimension plot of energy E vs energy loss ΔE. Fig.1 shows the result using a carbon target alone and Fig.2 shows the result using lithium carbonate with the carbon backing. In Fig.2 scattered protons and deuterons are well separately observed as two lines. The groups A, B, C, D, E and F correspond to the reactions ^{6}Li(^{3}He,p$_0$)^{8}Be, ^{6}Li(^{3}He,p$_1$)^{8}Be, ^{7}Li(^{3}He,p$_0$)^{9}Be, ^{7}Li(^{3}He,p$_1$)^{9}Be, ^{12}C(^{3}He,p)^{14}N and ^{7}Li(^{3}He,d)^{8}Be, respectively.

Since the natural lithium contains 92.5% of ^{7}Li and 7.5% of ^{6}Li, and Q-value of (^{3}He,p) reaction is higher for ^{6}Li than ^{7}Li, which are 16.78 MeV and 11.20 MeV, respectively, the protons scattered from ^{6}Li are quite disturbing. More progressive studies are planned to measure the astrophysical S-factors for the reaction ^{7}Li(^{3}He,p)^{9}Be with more lower energy beam and an enriched isotope target.

References

[1] Asplund, M., Lambert, D. L., Nissen, P. E., Primas, F., & Smith, V. V. 2006, Apj, 644, 229.

[2] M. Kusakabe et al.,Astrophys. J. 680. 846-857(2008).

[3] J. Yan et al., Phys. Rev. C65 (2002) 048801.

[4] D. P. Rath et al., Nucl. Phys. A515, 338 (1990).

[5] M. F. Werby and S. Edwards, Nucl. Phys. A213, 294 (1973).

[6] R. L. Dixon and R. D. Edge, Nucl. Phys. A156, 33 (1970).

2.2 The study of nucleosynthesis by means of scandium-45 + p reaction

T. Onishi, T. Komatsubara, T .Yuasa, K. Sasa, S .Kubono[1], T. Hayakawa[2], and T. Shizuma[2]

Elements lighter than iron are created by the following process in stars. At initial stage of nucleosynthesis, p-p chain, triple-alpha reaction and alpha-burning occur. Subsequently, carbon, oxygen, neon and silicon burning proceed in massive star and various elements to iron are created. We took an interest in silicon burning. The silicon burning starts from photodisintegration by high-energy gamma-ray and alpha-capture of silicon. Then, various elements are created through quasi-equilibrium process. The reaction flow of quasi-equilibrium process is complex and there are many reactions around scandium-45 [1]. The aim of our study is to measure reactions around scandium-45 which is known as a bottleneck in silicon burning. Woosly[1] pointed out that the flow is concentrated to ^{42}Ca(alpha,p)^{45}Sc and ^{45}Sc(p,gamma)^{46}Ti reaction. In order to evaluate nuclear reaction rate of the ^{42}Ca(alpha,p)^{45}Sc, we have performed measurements of the cross section for the inverse reaction of ^{45}Sc(p,alpha)^{42}Ca(Q-value = 2.34MeV). For this reaction, the experimental data were limited only above 2.8MeV [2]. Therefore, we measured ^{45}Sc(p,alpha)^{42}Ca reaction with proton beam of 2MeV. This energy corresponds to Gamow peak at a temperature of 3GK in silicon burning.

Our measurements were carried out by 1MV Tandetron accelerator at UTTAC. The proton beam of 2MeV was irradiated on scandium target. The scandium target was prepared by evaporation in vacuum on to 1.47 mg/cm^2 gold backing. The thickness of scandium layer was measured to be 0.2mg/cm^2. Alpha-particle from ^{45}Sc(p,alpha)^{42}Ca reaction was measured at angle of 148°with E-Δ E counter by using SSD. Accumulation of the measurement is about 7.5 hour.

As a result, alpha-particle from ^{45}Sc(p,alpha)^{42}Ca reaction was separately measured from strong elastic scattering of protons mainly by the gold backing. The yields of alpha-particle are corrected by dead time of DAQ and evaluated to be 67 counts. The relation of the yield and the cross section is represented by following equation,

$$Y = n\frac{N}{S}\frac{\mathrm{d}\sigma}{\mathrm{d}\Omega}\Omega$$

where Y is yield, n is number of incident proton, N/S is particle area density of scandium45, dσ/dΩ is differential cross section and Ω is solid angle. The differential cross section calculated by using this equation is

$$\frac{\mathrm{d}\sigma}{\mathrm{d}\Omega} = 0.0066 \pm 0.0010[\mathrm{mbarn/sr}]$$

at angle of 148°.

---

[1] Center for Nuclear Study, Univ. of Tokyo (CNS)

[2] Japan Atomic Energy Agency (JAEA)

Fig.1 shows the comparison of differential cross section between our result and the experimental data reported in ref [2] measured at 125°. Our result seems to be the value extrapolated to lower energy region of the previous reports. In Fig.2 the comparison of astrophysical S-factor is shown. The astrophysical S-factor of previous reports decreases as proton energy decrease and is lower than our result.

However, since many resonance structures can be expected, we are planning to perform measurements of detailed excitation function and angular distribution.

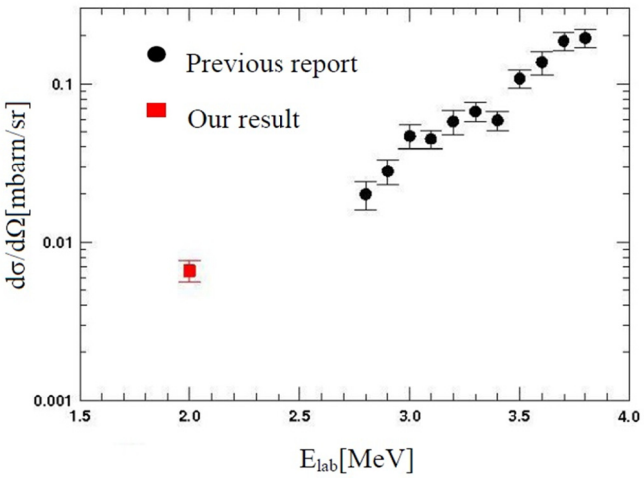

Fig.1. comparison of differential cross section

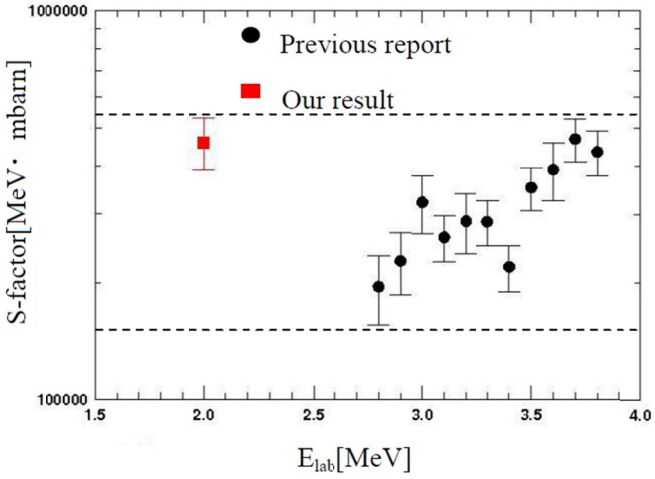

Fig.2. comparison of astrophysical S-factor

References

[1]S.E. Woosly, W. David Arnett, Donald D. Clayton Astrophys J.S.231,26(1973) 231-312

[2]J.S. Schweitzer, Z.E. Switkowaki, R.M. Wieland NPA 287 (1977) 344

3.

MATERIALS AND CLUSTER SCIENCE

3.1 Hydrogen uptake process in a-C:H film growth studied by RBS-ERDA with hydrogen isotope

D. Sekiba, N. Takemoto, M. Okada, S. Ishii, T. Sakurai, K. Akimoto

The hydrogen concentration in the hydrogenated amorphous carbon (a-C:H) film strongly affected the mechanical and electronic properties of the film. During the film deposition, H_2 gas is often added into the process gas such as CH_4 and C_6H_6 to control the hydrogen concentration, though the origin of the hydrogen in the film has not been well understood. We investigated the hydrogen uptake process during the a-C:H film deposition by using D_2 and CH_4 to distinguish the origin of hydrogen. The concentration of H and D in the film was determined by elastic recoil detection analysis (ERDA) [1].

The films were deposited on the Si substrate by reactive RF magnetron sputtering with D_2 and CH_4. The RF power and frequency were set at 150 W and 13.6 MHz, respectively. The typical thickness of the film is ~ 200 nm. The partial pressure of CH_4 and Ar were set at 1.6×10^{-1} Pa and 4.0×10^{-2} Pa, respectively, while that of D_2 was changed between $0.25 \times 10^{-2} \sim 10.0 \times 10^{-2}$ Pa. ERDA and Rutherford backscattering spectroscopy (RBS) were taken at the 1MV Tandetron in UTTAC. The 2.5 MeV $^4He^{2+}$ ions were irradiated to the sample with the angle of 75 degree from the surface normal. The recoiled and backscattered particles were detected by Si surface detector (SSD) at the angles of 30 and 150 degree with respect to the beam incident direction. The schematics of the setup are found elsewhere [2].

Figure 1 shows the determined H and D concentration as a function of partial pressure ratio of D_2 with respect to the total pressure. We can see that the D concentration in the film is linearly increased with increasing the D_2 molecules in the chamber. On the other hand, H concentration decreases with decreasing the CH_4 molecules in the chamber, so that the total concentration of H+D is almost constant independently of the D_2 partial pressure. We can conclude that the H atom is provided both from CH_4 and H_2 in the process gas and the degree of the contribution is determined by the number of molecules instead of the number of atoms.

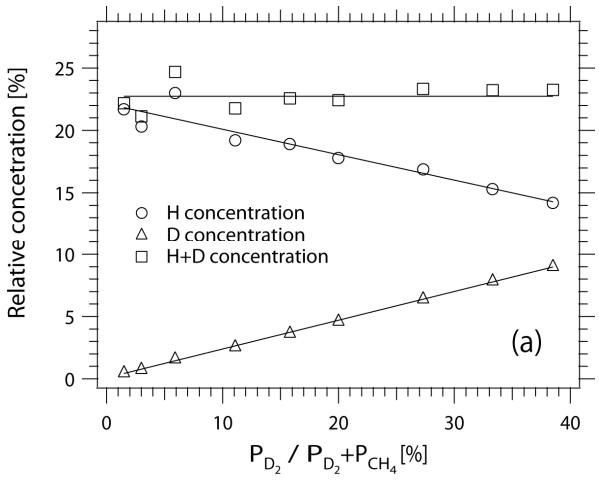

Fig.1. H and D concentration as a function of partial pressure of D_2 in the process gas.

References

[1] D. Sekiba, N. Takemoto, M. Okada, S. Ishii, T. Sakurai, K. Akimoto, Diamond and Related Materials, 27-28 (2012) 60-63.

[2] D. Sekiba, M. Horikoshi, S. Abe, S. Ishii, Journal of Applied Physics 106 (2009) 114912.

3.2 Droplet formation in $N_2/H_2O/SO_2$ by corona discharge

I. Harayama, H. Tanikawa, S. Funada, K. Sasa and S. Tomita

In 2000, it was reported by Svensmark *et al*. [1] that the intensity variations of galactic cosmic ray (GCR) could have certain correlation with the coverage of earth's surface by low-level clouds in the atmosphere. As a possible key process of the correlation, the process of aerosol formation induced by GCR has attracted attentions. A fraction of these aerosols could grow as cloud condensation nuclei, which would enhance the earth's coverage by low-level clouds. To investigate the aerosol formation process by GCR, we have measured the small droplet formation by 20 MeV protons, and shown that oxidation process of SO_2 play an important role. Sulfuric acid (H_2SO_4) is known as an important component for the nucleation process [2], which is normally produced from SO_2 in the atmosphere through the oxidation process. In order to improve our knowledge of the mechanism, we plan to generate droplets with a corona discharger where only unipolar ions are generated. The experiment study using the corona discharger would help us to understand the role of positive and negative ions in the oxidation process. In this report, we show our preliminary results with new experimental apparatus using a corona discharger.

The schematic drawing of the corona discharger is shown in Fig. 1. The corona discharger had a needle and a plate electrode with a hole of 3 mm in diameter. As the needle electrode, we employed a stainless steel pin which was held at high voltage of a few kV so that corona discharge takes place. The electrical mobility of the generated aerosols in the sample gas was measured by a differential mobility analyzer (DMA), and SO_2 analyzer (Thermo, Model 43i) was used to measure concentration of SO_2.

The time variation of the concentration of SO_2 in the sample gas is shown in Fig.2. It is clearly seen that the concentration of SO_2 becoming lower while corona discharge takes place. This means that the consumption of SO_2 is caused by the oxidation process of SO_2. The typical spectrum of electrical mobility of aerosols with same experimental condition is shown in Fig. 3. The spectrum has a peak around electrical mobility of 5×10^{-6} m^2/Vs. The droplet density can be obtained by integrating the spectrum. We plan to study more detail on the relationship between consumption of SO_2 and droplet density.

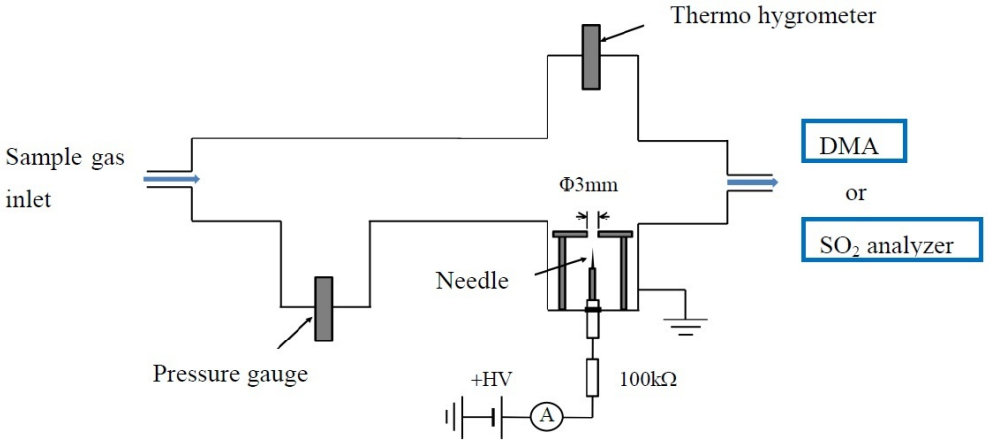

Fig.1. The schematic of corona discharger.

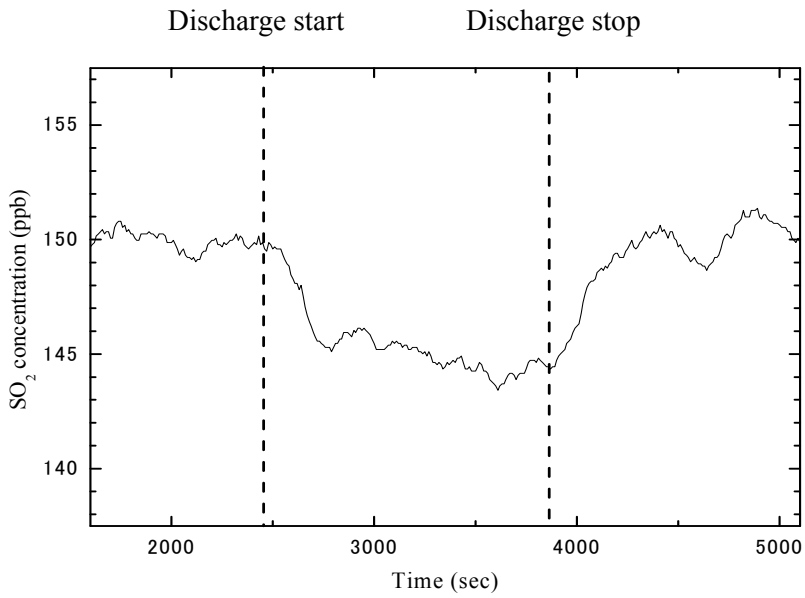

Fig.2. The concentration of SO_2 in sample gas. The corona current was 4.0 μA.
The measured relative humidity of the sample gas was 30%, and the concentration of SO_2 was 150 ppb.
The broken lines indicate the times when corona discharge started and stopped.

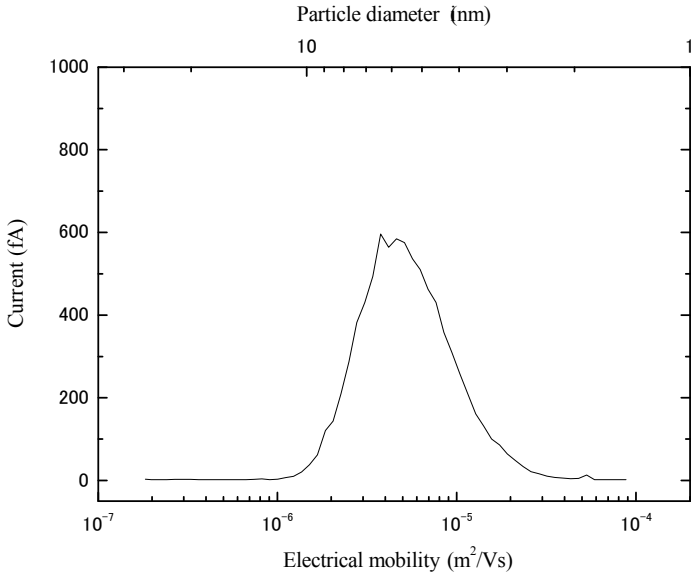

Fig.3. The spectrum of electrical mobility of droplets. The corona current was 4.0 μA.
The measured relative humidity of the sample gas was 30%, and the concentration of SO_2 was 150 ppb.

References

[1] N D. Marsh and H. Svensmark, Low Cloud Properties Influenced by Cosmic Rays. *Phys. Rev. Let*. **85**, 5004-5007, 2000

[2] John H. Seinfeld and Spyros N. Pandis, *Atmospheric Chemistry and Physics: From Air Pollution to Climate Change, Second Edition*. John Wiley & Sons, Inc, 2006

3.3 Measurement of secondary electron yields with a micro-channel plate for the study of cluster effects

Y. Shiina, S. Tamura, I. Harayama, K. Yamazaki, K. Sasa, S. Ishii and S. Tomita

When fast cluster ions impinged on a material surface, the secondary electron yields are suppressed strongly compared to those of atomic ions [1]. This is an example of phenomena called cluster effects. It is already known that cluster effects on energy losses are so weak compared with those on secondary electron yields [2], while secondary electron yields under irradiation of atomic ions are known to be proportional to their electronic energy loss over a broad range of energy and target material [3]. Therefore, it seems that the cluster effect on secondary electron emission stems mainly from the transport or transmission process, rather than the production process. But the details of the suppression mechanism are not understood yet. For the further investigation, the coincidence studies with, for example, the orientation of injected molecules, and inter atomic distance between the constituent atoms are thought to be important.

We recently constructed a new experimental setup with a micro-channel plate (MCP) together with an SSD, which enables us event-by-event measurements of secondary electron yields in coincidence with scattered ions. This report is the result of test measurements with fast protons and carbon cluster ions.

The experimental setup is shown in Fig. 1. Projectiles were delivered from the 1 MV Tandetron accelerator at UTTAC. The accelerated ions were injected to a thin carbon foil of 5.3 μg/cm^2 in thickness. At the downstream of the target, an SSD was placed for the detection of transmitted ions. On the other side of the target, a grid was placed and held at +200 V, so that the secondary electrons were extracted and injected into the MCP. The secondary electron yield is obtained event by event by measuring the integration of the MCP signal using a charge sensitive amplifier. The measured secondary electron yields of proton injection (0.5 - 1.7 MeV) are shown in Fig. 2 as a function of electronic stopping power calculated with SRIM code. The results agree with those reported by Rothard *et al*. [3]. We also performed the same experiment with fast carbon clusters (0.5 MeV/atom, cluster size n = 1 - 4), and the results are shown in Fig. 3 as a function of cluster size. It is clearly seen that the secondary electron yield decreases as the number of ions in a cluster increases. The reduction of the secondary electrons agrees quite well with that reported by Arai *et al*. [1].

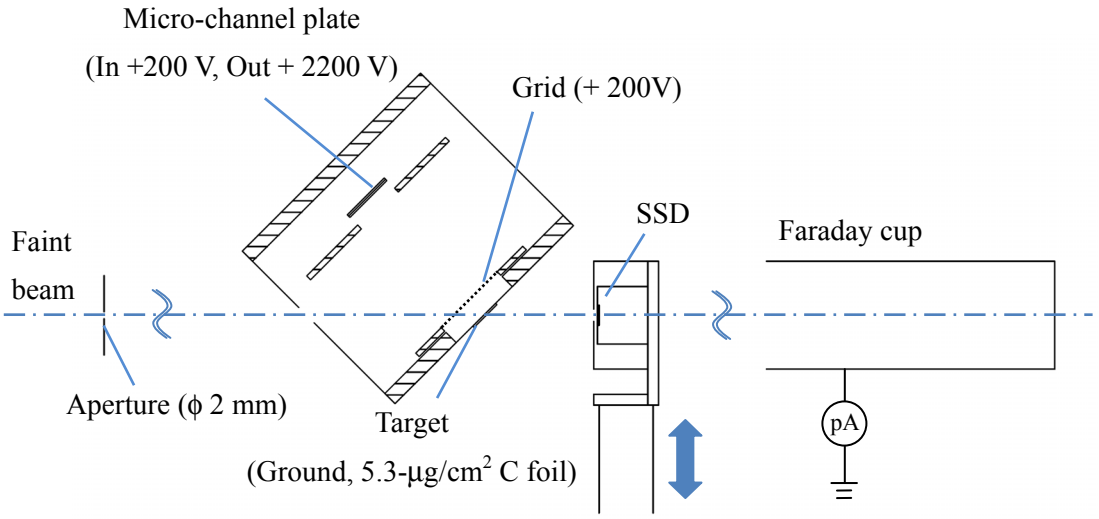

Fig. 1. A schematics of the experimental setup

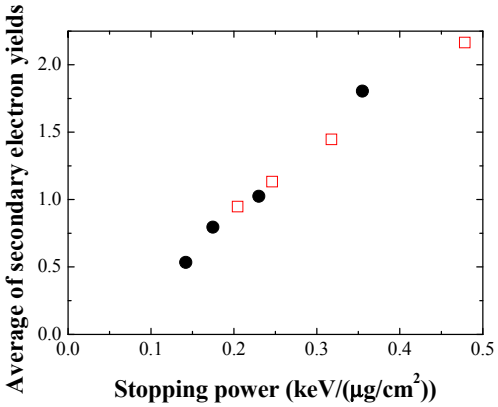

Fig. 2. Stopping power dependence of secondary electron yields by protons: the circles are the present data, and the squares are the results reported by Rothard *et al*. [3].

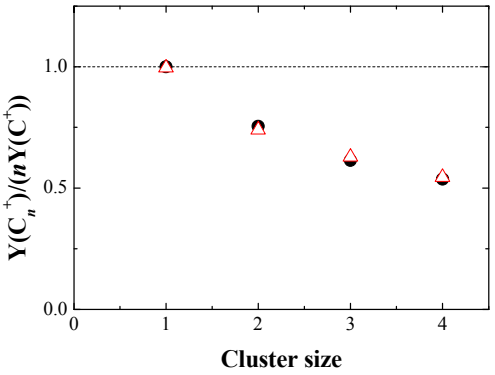

Fig. 3. Cluster size dependence of secondary electron yields per atom by carbon clusters: the circles are the present data, and the triangles are the results reported by Arai *et al*. [1].

References

[1] H. Arai, H. Kudo, S. Tomita and S. Ishii, *J. Phys. Soc. Jpn*. **78**, 104301 (2009).

[2] S. Tomita, M. Murakami, N. Sakamoto, S. Ishii, K. Sasa, T. Kaneko and H. Kudo, *Phys. Rev.* A **82**, 044901 (2010).

[3] H. Rothard, K. Kroneberger, A. Clouvas, E. Veje, P. Lorenzen, N. Keller, J. Kemmler, W. Meckbach and K. O. Groeneveld, *Phys. Rev.* A **41**, 2521 (1990).

[4] H. Rothard, K. Kroneberger, M. Burkhard, J. Kemmler, P. Koschar, O. Heil, C. Biedermann, S. Lencinas, N. Keller, P. Lorenzen, D. Hofmann, A. Clouvas, K. O. Groeneveld and E. Veje, *Radiat. Eff. Defects Solids* **109**, 281 (1989).

3.4 Investigation of layer thicknesses in CaF_2/Fe_3Si heterostructures grown on Si(111) substrates by molecular beam epitaxy

K. Harada, K. Toko, T. Suemasu, N. Takemoto, S. Ishii, M. Matsumura, S. Yamazaki, D. Sekiba

Introduction

Ferromagnetic silicide Fe_3Si is an attractive material for Si-based spintronics applications because the lattice parameter of Fe_3Si is 0.564 nm, which nearly lattice-matches Si. Furthermore, Fe_3Si has a relatively high Curie temperature of approximately 803 K [1]. We have achieved a magnetoresistance (MR) ratio of 0.28% at room temperature (RT) in the $Fe_3Si/CaF_2/Fe_3Si$ magnetic tunnel junction (MTJ) structures [2]. To enhance the MR ratio, we need to process the MTJs into a much smaller-sized mesa structure to avoid inclusion of defects in the device area using the Ar ion milling technique. Thus, it is important to know the exact thickness of each layer in the MTJs. For this purpose, we attempted to evaluate the thickness of layers in the MTJs by Rutherford backscattering spectrometry (RBS) measurement. The integrated intensity of RBS spectrum depends on the thickness of layers.

Experimental

We fabricated four MTJs samples by molecular bean epitaxy (MBE). Growth conditions of samples by MBE were summarized in Table 1. $Fe_3Si/CaF_2/Fe_3Si$ MTJ structures are for samples A, B and C, $Fe/CaF_2/Fe_3Si$ MTJ structure is for sample D. The thickness of each layer in these samples was determined by RBS measurement using SIMNRA at the C-course of the 1MV Tandetron accelerator in UTTAC.

Table 1 Growth condition of samples.

Sample	Thermal cleaning	Sub.	Si buffer		CaF_2 buffer	
			Deposition	Annealing	Deposition	Annealing
Sample A	15 min 800 ˚C (Si supplying)	n-FZ Si(111) (1000-5000 Ω･cm)	10 nm 350 ˚C	20 min 1000 ˚C	5 nm 280 ˚C	20 min 300 ˚C
Sample B						
Sample C						
Sample D			–	–		

Sample	Fe_3Si bottom layer		CaF_2 barrier layer		Fe_3Si top layer		Fe layer	Pt layer
	Deposition	Annealing	Deposition	Annealing	Deposition	Annealing		
Sample A	15 nm 80 ˚C	20 min 300 ˚C	2 nm 280 ˚C	-	9 nm 80 ˚C	30 min 280 ˚C	9 nm ~ 40 ˚C	3 ~ 5nm ~ 40 ˚C
Sample B	15 nm 130 ˚C			20 min 300 ˚C	10 m 80 ˚C	30 min 250 ˚C	10 nm ~ 40 ˚C	
Sample C	15 nm 130 ˚C		5 nm 280 ˚C	20 min 300 ˚C	15 nm 130 ˚C	20 min 300 ˚C	15nm ~ 40 ˚C	
Sample D	15 nm 130 ˚C		2 nm 200 ˚C	-	-	-	15nm ~ 40 ˚C	

Results and Conclusion

Figure 1 shows the RBS spectra of the samples. Pt, Fe, Ca and Si spectra were clearly observed in each sample. We next estimated the thickness of each layer in the MTJs using SIMNRA. The RBS spectra were well fitted by the calculation. Table 2 shows the results of calculation for each sample. Reasonable results were obtained from these calculations in comparison with the growth conditions shown in Table 1.

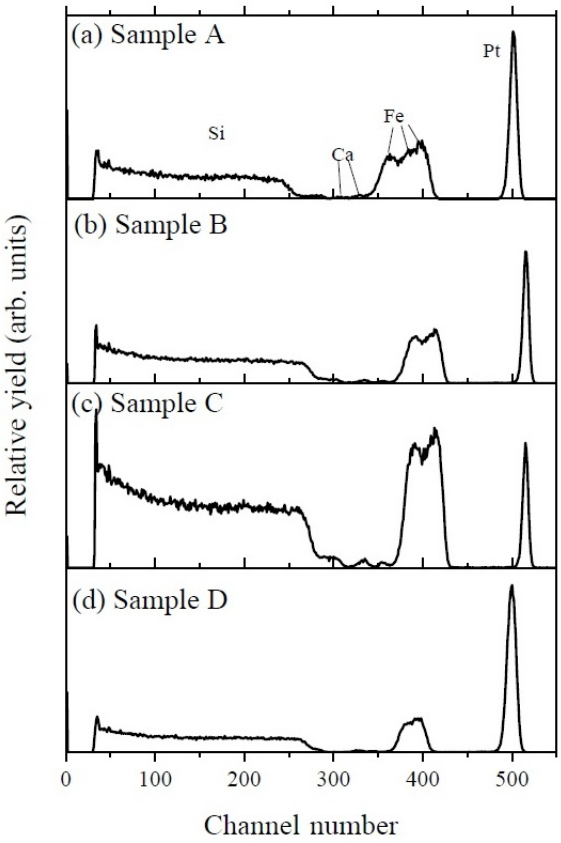

Fig. 1 RBS spectra of samples A-D.

Table 2 Layer thickness (nm) in samples A-D investigated by RBS.

Layer	Sample A	Sample B	Sample C	Sample D
Pt layer	2.3	0.78	4.0	7.1
Fe layer	8.4	10.0	17.6	13.6
Fe_3Si top layer	8.8	10.1	12.1	-
CaF_2 barrier layer	1.3	0.77	2.1	0.65
Fe_3Si bottom layer	18.1	17.3	18.9	12.9
CaF_2 buffer layer	6.5	3.7	1.3	2.0
Si(111) sub.				

References

[1] A. Ionescu, C. A. F. Vaz, T. Trypiniotis, C. M. Gürtler, H. Garcia-Míquel, J. A. C. Bland, Phy. Rev. B **71** (2005) 094401.

[2] K. Harada, K. S. Makabe, H. Akinaga, and T. Suemasu, J. Phys. Conference Series **266** (2011) 012088.

3.5 Conversion electron Mössbauer spectroscopy (CEMS) study of an iron oxide thin film fabricated by reactive sputtering

M. Minagawa[1], M. Myoka, H. Yanagihara and E. Kita

Iron oxides with spinel structures have been studied by many researchers since the beginning of the magnetism research. The physical and magnetic properties of iron oxides can be controlled by using additional elements, and thus, magnetic materials with various magnetic characteristics from hard to soft magnetism can been realized. For modern applications of magnetic materials, such as high-density magnetic recording media and spintronics devices, thin films are highly desired. Hence, thin films of spinel ferrites have been fabricated by a variety of techniques such as chemical vapor deposition (CVD) in early years, and reactive vapor deposition in which atomically-flat surfaces were achieved[1].

In the previous works, we have used O_2 and/or O_3 gas as reaction sources in the molecular beam epitaxy (MBE) and obtained Fe_3O_4 and γ-Fe_2O_3 epitaxial films[2]. Metastable γ-Fe_2O_3 was only obtained in the films with limited thickness[3] of less than 130 Å and these films' good quality resulted in antiferromagnetic interlayer couplings in Fe/Fe_3O_4 or Fe/MgO/γ-Fe_2O_3 epitaxial films. The coupling energy was about 1.5 erg/cm^2, which is sufficient for a soft underlayer (SUL) in perpendicular magnetic recording media that are used in a hard disk drive, and the multilayers will be an alternative to the Co/Ru/Co antiferromagnetically coupled system. From the viewpoint of practical thin-film fabrication, sputtering has many advantages over vacuum deposition. As the first step, we have prepared epitaxial $Fe_{3-\delta}O_4$ films by employing rf magnetron sputtering and have determined their degree of oxidation using Mössbauer spectroscopy.

A conventional multi-target rf sputtering system (ULVAC Inc.) was used for the sample preparation with a metallic iron target. The flow rates of sputtering gases were controlled at 30 sccm for Ar and at 1.5 sccm for the reactive gas, O_2. The film was grown on the MgO (100) single crystal substrate, and the film thickness was about 460 Å. The single crystal growth was confirmed by RHEED observation just after the deposition. Mössbauer measurements were carried out with standard conversion electron Mössbauer Spectroscopy(CEMS) at room temperature. Hyperfine fields and isomer shifts were calibrated via a standard α-Fe spectrum recorded at room temperature. Data were analyzed with a commercial least squares fitting program (MossWinn 3.0).

Figure 1 shows a CEMS spectrum of the $Fe_{3-\delta}O_4$ film. The spectrum was fitted to a single hyperfine subspectrum with a hyperfine field of 487 kOe and an isomer shift of 0.33 mm/s, which are attributed to Fe^{3+} ions of γ-Fe_2O_3. It is noted that the spectrum was fairly symmetric about the center of the spectrum, which implies a simple configuration of the spectrum. However, the hyperfine field strength was slightly smaller than the previously reported value 499 kOe for a bulk-like material[4]. There may be room for improvement in the degree of oxidization and/or the ordering of B site vacancies.

In the previous work, we fabricated γ-Fe_2O_3 thin films using a reactive vapor deposition technique with O_3 gas[2,3]. In the present work, we have fabricated γ-Fe_2O_3 thin films with the reactive sputtering technique without using a special gas such as O_3. Since this technique does not require a special gas, it is

[1]present address: Itami works, Sumitomo Electric Industry Ltd.

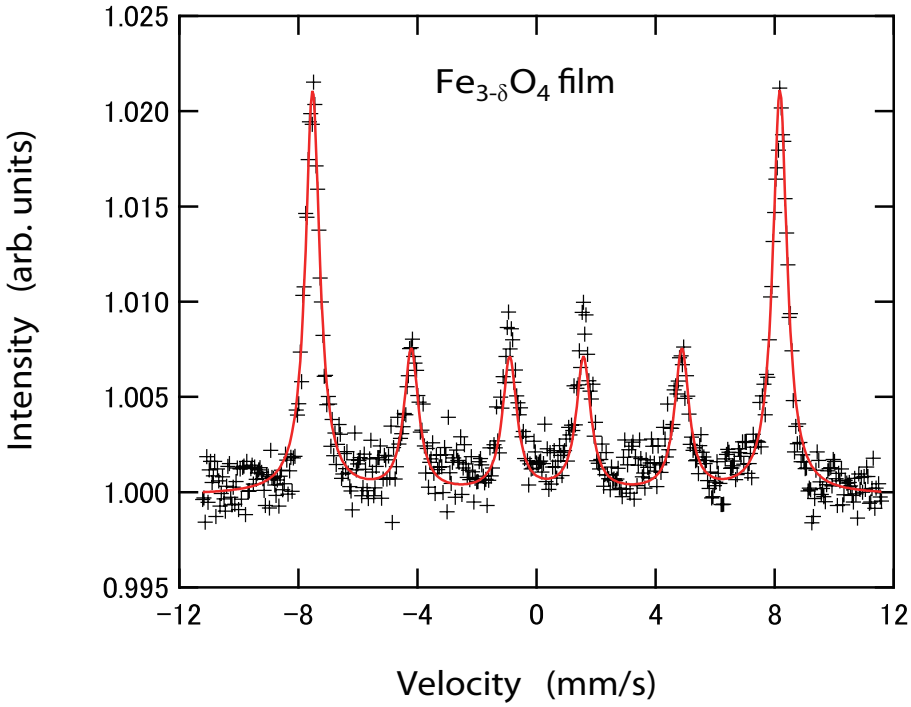

Fig. 1. CEMS spectrum of an iron oxide thin film prepared by reactive sputtering. This spectrum was fitted to a single magnetic subspectrum with the hyperfine field of 487 kOe. The solid line shows the fitting result.

advantageous for growing spinel-type ferrite oxide thin films.

References

[1] Yuri Suzuki: Annu. Rev. Mater. Res. **31** (2001) 265.

[2] Y. Yanagihara *et al.*: J. Appl. Phys. **101** (2007) 09D101.

[3] M. Minagawa *et al.*: Jpn. J. Appl. Phys. **49** (2010) 080216.

[4] E. Murad, in *Iron in Soils and Clay Minerals*, J. W. Stucki, B. A. Goodman, and U. Schwertmann, eds., Reidel, Dordrecht, (1987)

3.6 Mössbauer analysis of Mg-containing Fe_3O_4 nanoparticles for magnetic hyperthermia

D. Isaka, M. Kishimoto, H. Yanagihara, E. Kita

Magnetic nanoparticles have attracted much attention because of their potential to generate heat in magnetic hyperthermia and thermoablation for cancer therapy. The origin of magnetically generated heat from inductive mediators essentially depends on the size and magnetic properties of the particles. Hysteresis loss is a dominant mechanism of heat generation for ferromagnetic and ferrimagnetic particles. We have been studying ferromagnetic nanoparticles, especially cobalt-doped magnetite particles, as high heat generating materials for magnetic hyperthermia and thermoablation [1]. We must consider the biocompatibility of magnetic materials for their practical use. The biocompatibility of other elements than iron, cobalt in particular, must be carefully checked, even when they are used as dopants. Although cobalt toxicity is not fully understood, preparing cobalt-free particles is beneficial for safety aspects. In the present study, we synthesized Mg-containing iron oxide particles.

Spinel-structured Mg-containing iron oxide nanoparticles, $(Mg)Fe_3O_4$, were synthesized by coprecipitation and a hydrothermal process. We have labeled the various nanoparticle samples MTH0 through MTH6 corresponding to the increasing Mg content from 0 to 10.0 at% with respect to the total Fe content: the 10 at% concentration corresponds to $Mg_{0.33}Fe_{2.67}O_4$. Magnetization of dry powdered samples was measured using a vibration sample magnetometer (VSM). Particle size and crystal structure were obtained using X-ray diffraction (XRD). Mössbauer spectra were recorded at room temperature and were numerically analyzed using commercially available fitting software, MössWinn 3.0.

The basic characteristics of the $(Mg)Fe_3O_4$ particles in the various samples are summarized in Table 1. The magnitude of the coercive forces peaked for the MTH1 sample and then decreased with increasing Mg content for the other samples.

Table 1. Characteristics of $(Mg)Fe_3O_4$ particles.

Sample	Mg content at%	D_{XRD} (nm)	H_c (Oe)	M_s (emu/g)
MTH0	0	41	141	85
MTH1	2.0	33	155	77
MTH2	3.2	24	136	70
MTH3	4.0	21	109	68
MTH4	6.0	18	71	63
MTH5	8.0	15	41	54
MTH6	10.0	14	40	51

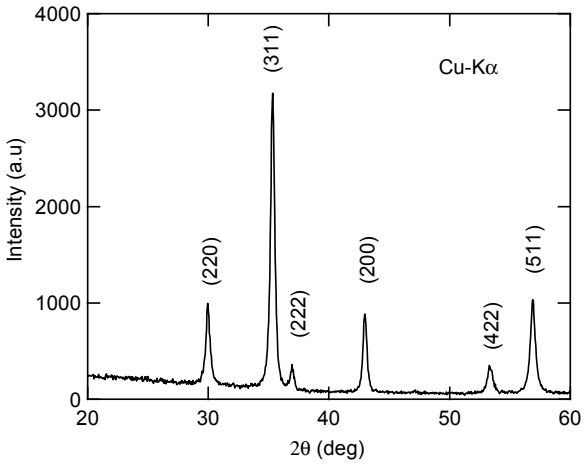

Fig. 1. XRD profile for $(Mg)Fe_3O_4$ MTH2 particles with 3.2 at% Mg.

Figure 2 shows the typical Mössbauer spectra for (Mg)Fe_3O_4 particles. The solid lines indicate the fitted results. For all synthesized particles, the spectra composed of two ferromagnetic subspectra, and an additional broad peak is present in the spectra for the MTH5 and MTH6 samples. The magnetic subspectrum with the higher hyperfine field (H_{hp}) is attributed to the Fe^{3+} ions in tetrahedral sites (A sites) and the other sextet to the Fe^{2+} and Fe^{3+} ions in the octahedral sites (B sites). The subspectrum with the broad linewidth observed for MTH5 and MTH6 was fitted to a doublet and was attributed to the superparamagnetism caused by relatively small particle volumes.

The Mg atom distribution can be estimated from the area ratios of the subspectra. Mg atoms tend to occupy B sites in the thin Mg concentration region below $Mg_{0.5}Fe_{2.5}O_4$ [2]. To determine the occupation, Mössbauer analyses have been generally performed at 77 K or lower. As seen in Fig. 2, the higher concentration Mg samples contain the superparamagnetic component because of the small particle sizes. Therefore, low-temperature measurements are highly desirable in this work compared to previous works.

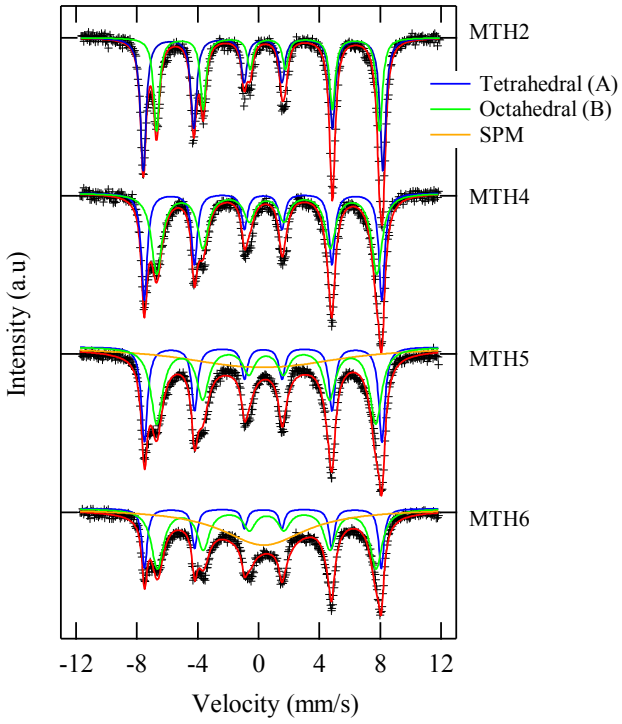

Fig. 2. Mössbauer spectra recorded at room temperature for MTH2, MTH4, MTH5, and MTH6. Solid lines indicate fitted results.

The heating characteristics of the dry MTH2 and (Co)Fe_3O_4 samples, which had the same coercive force (~140 Oe), were measured with an 120 kHz alternating magnetic field produced using a high-frequency magnetic field applicator with a field amplitude of H_0 = 400 Oe. The specific loss power (SLP) of the nanoparticles was evaluated by assuming that the total heat capacity included those of the magnetic particles and the water suspension sample. The SLP was then calculated using $\Delta T/\Delta t$. The SLPs of the (Mg)Fe_3O_4 and (Co)Fe_3O_4 particles were 51 and 42 W/g, respectively. The experimentally obtained SLP was consistent with the estimated loss power represented by the minor loop.

References

[1] E. Kita *et al*., *J. Phys. D: Appl. Phys*. **43** (2010) 474011.

[2] F. Nakagomi *et al*., *J. Solid State Chem.* **182** (2009) 2423.

4.

INTERDISCIPLINARY RESEARCH

4.1 Direct Characterization of Hydrogen Content in MLCC employing Elastic Recoil Coincidence Spectrometry

K. Morita[1], Y. Iwazaki[1], H. Kishi[1], D. Sekiba and T. Komatsubara

Introduction

Hydrogen location has been recognized to be associated with the insulation properties in perovskite system. Recently the first principle calculation by Iwazaki *et al*. has revealed that hydrogen atoms could be trapped at oxygen vacancy sites with negative ions, H^- (effectively negative single-charge, H′, according to the Kröger-Vink notation) when the electron carrier density in perovskite oxides is remarkably high [1]. The calculation explains the recent experimental results that the hydrogen doping into Nb-doped or oxygen-deficient $SrTiO_3$ single crystals could decrease their high conductivity [2, 3]. Thus, a possible hydrogen-incorporation during the heat treatment in forming gas can be considered to be of great concern for the fabrication of thin-film-functional-devices based on perovskite oxides [4].

Some of the perovskite oxide ceramics are used as dielectric materials for multilayer ceramic capacitors (MLCCs). Nevertheless, the influence of hydrogen incorporation on insulation properties for the MLCCs has never been sufficiently elucidated. In particular, $BaTiO_3$-based MLCCs with Ni internal electrodes (Ni-MLCCs) are fired in a reducing atmosphere consisting of H_2, N_2 and H_2O to prevent the Ni electrodes from oxidation. Since hydrogen in the atmosphere could be partly incorporated into the $BaTiO_3$-based ceramics during the firing, it becomes important to know hydrogen content in Ni-MLCCs in order to ensure the insulation properties.

In this report, we show the characterized results of the hydrogen content in Ni-MLCCs employing elastic recoil coincidence spectrometry (ERCS). It is concluded that the hydrogen content is negligibly small an 5 μm. Some of the as-fired MLCCs were then oxidized at 1000°C in a mildly oxidizing atmosphere (Po_2 = 30 Pa). Moreover, some of the as-fired and oxidized MLCCs were heat-treated (600°C, 1 hour) in forming gas with the intent for hydrogen to be doped into the MLCCs.

Electrical characterization: The temperature dependence of permittivity and dielectric dissipation factor (tanδ) of the MLCCs were measured at 1.0 kHz and 1.0 Vrms using an impedance analyzer (Model 4284A; Agilent, USA). The current-voltage (*I-V*) characteristics of the MLCCs were measured at 25°C and 150°C using an ultra-high resistance meter (Model R8340; Advantest, Japan). The current-time (*I-t)* characteristics under the dc-electric field of 20 V/μm were recorded at 150°C.

ERCS hydrogen analysis: Proton-proton ERCS was employed to measure hydrogen content in the MLCCs. ERCS using proton beam is nondestructive as well as highly sensitive for the detection of hydrogen atoms [5]. Fig. 1 illustrates a typical geometry of the measurement system. In the ERCS system, the Ni-MLCC was irradiated with a 20 MeV proton beam, and recoiled protons in the MLCC and forward-scattered incident protons were simultaneously detected by two silicon surface-barrier detectors. In principle, two directions of the elastically scattered particles with the same mass form 90° in non-relativistic kinematics. Therefore, the two detectors were installed at ±45° with respect to the incident beam so that a recoiled

[1] General R&D Laboratories, Taiyo Yuden Co., Ltd.

proton by an incident proton can be exclusively detected as a coincidence event with the detection of the forward-scattered incident proton. The beam current and the beam size on the MLCCs were approximately 120 pA and 0.3×0.4 mm^2, respectively. The ERCS spectra were analyzed and the hydrogen content was estimated using the Mylar films as the chemical standard.

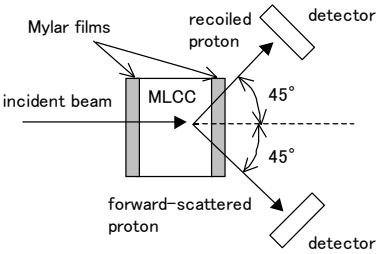

Fig. 1: Geometry of a measurement system for proton-proton ERCS.

Results and Discussion

Characterization of Electrical property: No measurable differences were observed on permittivity and dielectric dissipation factor (tanδ) over a wide temperature range between as-fired and oxidized MLCCs, implying that the oxidation treatment did not influence on ferroelectric domain motion of the $BaTiO_3$-based ceramics. However, the *I-V* and *I-t* characteristics of those MLCCs are remarkably affected by the oxidation treatment. The oxidized MLCC exhibited much lower current than that of the as-fired MLCC. The current for the oxidized one kept stable for more than 10000 seconds, though, those for the as-fired one broke down as soon as the measurement started. These results imply that the insulation properties can be attributed to oxygen vacancies generated during the firing. In the firing process, when the $BaTiO_3$-based ceramics were reduced, electrons as twice many as oxygen vacancies could be introduced into the perovskite lattice as follows:

$$O_o^X \rightarrow V_o^{\bullet\bullet} + 2e' \quad (1)$$

where O_o^X and $V_o^{\bullet\bullet}$ represent an oxygen atom in the lattice and an oxygen vacancy with the effectively positive double-charge, respectively. The oxidizing treatment decreases the amount of both oxygen vacancies and electrons, resulting in the decrease of leakage current. Furthermore, the decrease in oxygen vacancies provides MLCCs with longer lifetime since electro-migrations of oxygen vacancies are predominant cause for insulation-degradation with time for MLCCs [6, 7]. However, if there is a remarkable change in hydrogen content before and after the oxidation treatment, the contributions of hydrogen to the insulation properties should be considered. When hydrogen atoms are incorporated into the $BaTiO_3$-based ceramics without the influence of oxygen vacancies, electrons can be generated as follows:

$$H_2 \rightarrow 2H_i^{\bullet} + 2e' \quad (2)$$

where $H_i^{\bullet}$ represent an interstitial hydrogen atom with the effectively positive single-charge in perovskite lattice. Therefore, we need to know hydrogen content to pursue the exact cause of leakage current in Ni-MLCCs.

ERCS measurements: Mylar films with known hydrogen content were employed as standard samples. Fig. 2 shows proton counts as a function of channels, which corresponds to the sum energy of two protons detected, for the as-fired MLCC between the Mylar films. When a proton is scattered by another proton, the recoil energy becomes a half of the incident energy. Then the recoiled proton suffers larger energy loss because the stopping power increases by ~ 1.7 times for the half-energy protons. Since the sum of energy loss of recoiled protons is proportional to the depth measured from the exit side, the ERCS spectrum of Fig. 2 indicates the depth profile of hydrogen content. The signals at 350 Ch and 750 Ch are from the Mylar films of the incident and the exit sides, respectively, as illustrated in Fig. 1. The detection of protons from the Mylar film of the incident side shows that recoiled protons can be detected through the MLCC with 0.35 mm thickness. The hydrogen content inside the MLCCs was estimated by using the yields from the Mylar films as the calibration.

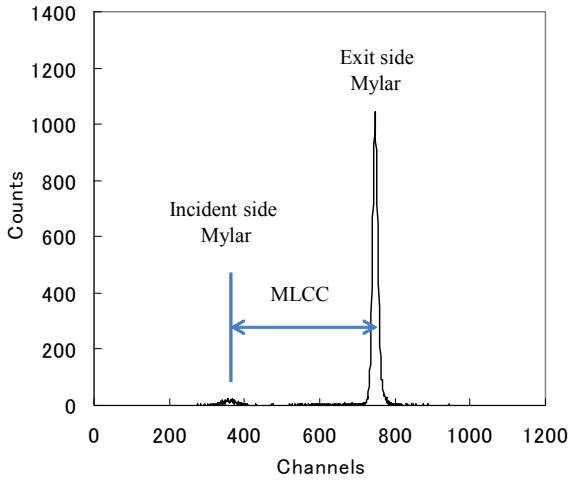

Fig. 2: ERCS spectrum for as-fired MLCC between two Mylar films. The signals around 350 Ch and 750 Ch are from Mylar films at the incident side and at the exit side, respectively.

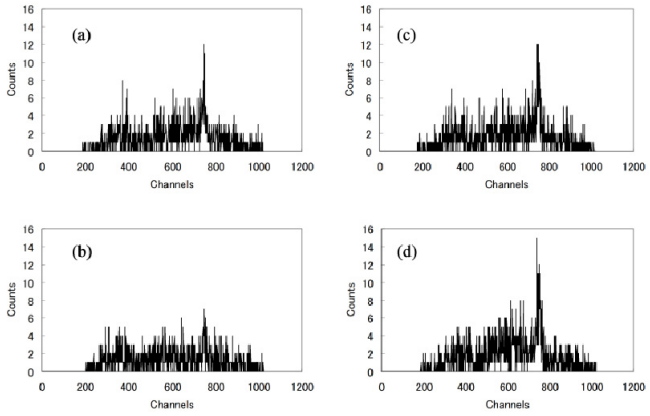

Fig. 3: ERCS spectra for (a) the as-fired and (b) the oxidized MLCCs. ERCS spectra for (c) the fired and (d) MLCCs after the heat treatment in forming gas.

The ERCS spectra of the as-fired MLCC and the oxidized MLCC without Mylar films are shown in Fig. 3 (a) and (b), respectively. The signals around 350 Ch and 750 Ch are from the contaminations on the MLCC surfaces. The signals from MLCC, which correspond to the region shown in Fig. 2, are very small compared to those from the surface contamination. The hydrogen contents estimated are 2.3 ± 0.1 ppm for the as-fired MLCC and 2.9 ± 0.1 ppm for the oxidized MLCC. It should be noted that the small amount of the yield is close to the measuring limit. In the same manner, we measured hydrogen content of the MLCCs via heat treatment in forming gas, and obtained ERCS spectra shown in Fig. 3 (c) and (d). The estimated values from these spectra are 2.8 ± 0.1 ppm for the as-fired MLCC and 3.2 ± 0.1 ppm for the oxidized MLCC. These results indicate that the hydrogen contents in Ni-MLCCs are maintained to be very small values close to the measurement limit irrespective of the

various atmospheres used in our experiments.

The estimated hydrogen content can be thought to be much smaller than the amount of oxygen vacancies in Ni-MLCCs. Whereas, G. Y. Yang et al. have revealed that the oxygen vacancies can be locally accumulated near the grain boundaries and cathodes in a concentration of ~ 10% for the resistance-degraded Ni-MLCC by dc electric field at elevated temperature [8]. Therefore, one can conclude that the influence of hydrogen on the insulation properties of Ni-MLCCs is negligible. On the other hand, several reports point out that hydrogen atoms incorporated into perovskite oxide ceramics, and the water-electrolysis can cause the insulation-degradation [9-11]. Thus the research on this viewpoint should be required to elucidate the role of hydrogen in Ni-MLCCs.

Acknowledgements

The present study was conducted under the support of the project 'Open Advanced Facilities Initiative for Innovation (Strategic Use by Industry)' of Ministry of Education, Culture, Sports, Science and Technology (MEXT), Japan.

References

[1] Y. Iwazaki, T. Suzuki, and S. Tsuneyuki, J. Appl. Phys. 108 (2010) 083705.

[2] J. Y. Dai, W. P. Chen, G. K. H. Pang, P. F. Lee, H. K. Lam, W. B. Wu, H. L. W. Chan, and C. L. Choy, Appl. Phys. Lett. 82 (2003) 3296-3298.

[3] B. Jalan, R. Engel-Herbert, T. E. Mates, and S. Stemmera, Appl. Phys. Lett. 93 (2008) 052907.

[4] K. Morito, T. Suzuki, Y. Mizuno, I. Sakaguchi, N. Ohashi, and H. Haneda, Key Eng. Mater. 388 (2009) 167-170.

[5] T. Komatsubara, K. Sasa, K. Okumoto, S. Ishii, Y. Yamamoto, K. Satou, K. Furuno, and M. Kurosawa, Nucl. Instr. and Meth. in Phys. Res. B 251 (2006) 237-245.

[6] H. Chazono and H. Kishi, Jpn. J. Appl. Phys. 40 (2001) 5624-5629.

[7] K. Morita, Y. Mizuno, H. Chazono, and H. Kishi, Jpn. J. Appl. Phys. 41 (2002) 6957-6961.

[8] G. Y. Yang, E. C. Dickey, and C. A. Randall, J. Appl. Phys. 96 (2004) 7500-7508.

[9] W. P. Chen, X. P. Jiang, Y. Wang, Z. Peng, and H. L. W. Chan, J. Am. Ceram. Soc. 86 (2003) 735-37.

[10] W. P. Chen, L. T. Li, Y. Wang, and Z. L. Gui, J. Mater. Res. 13 (1998) 1110-12.

[11] M. Widerøe, R. Waser, and T. Norby, Solid State Ionics 177 (2006) 1469-1476.

5. LIST OF PUBLICATIONS

5.1 Journals

NUCLEAR PHYSICS

1. T. Yamaguchi, K. Tanaka,T. Suzuki, A. Ozawa, T. Ohtsubo, T. Aiba, N. Aoi, H. Baba, M. Fukuda,Y. Hashizume, K. Inafuku, N. Iwasa, T. Izumikawa, K. Kobayashi, M. Komuro, Y. Kondo, T. Kubo, M. Kurokawa, T. Matsuyama, S. Michimasa, T. Motobayashi, T. Nakabayashi, S. Nakajima, T. Nakamura, H. Sakurai, R. Shinoda, M. Shinohara, H. Suzuki, M. Takechi, E. Takeshita, S. Takeuchi, Y. Togano, K. Yamada, T. Yasuno, M. Yoshitake, Nuclear reactions of ^{19,20}C on a liquid hydrogen target measured with the superconducting TOF spectrometer, Nuclear Physics A **864,** 1-37 (2011).

2. Nozomi Sato, Hiromitsu Haba, Takatoshi Ichikawa, Daiya Kaji, Yuki Kudou, Kouji, Morimoto, Kosuke Morita, Kazutaka Ozeki, Takayuki Sumita, Akira Yoneda, Eiji Ideguchi, Hiroyuki Koura, Akira Ozawa, Tsutomu Shinozuka, Takayuki Yamaguchi, and Atsushi Yoshida, Production and Decay Properties of ^{264}Hs and ^{265}Hs, J. Phys. Soc. Jpn., Vol.**80,** 094201 (2011).

3. K. Minamisono, T. Nagatomo, K. Matsuta, C. D. P. Levy, Y. Tagishi, M. Ogura, M. Yamaguchi, H. Ota, J. A. Behr, K. P. Jackson, A. Ozawa, M. Fukuda, T. Sumikama, H. Fujiwara, T. Iwakoshi, R. Matsumiya, M. Mihara, A. Chiba, Y. Hashizume, T. Yasuno, and T. Minamisono, Low-energy test of second-class current in β decays of spin-aligned ^{20}F and ^{20}Na, Phys. Rev. C **84**, 055501 (2011).

4. A. Ozawa, Y. Hashizume, Y. Aoki, K. Tanaka, T. Aiba, N. Aoi, H. Baba, B. A. Brown, M. Fukuda, K. Inafuku, N. Iwasa, T. Izumikawa, K. Kobayashi, M. Komuro, Y. Kondo, T. Kubo, M. Kurokawa, T. Matsuyama, S. Michimasa, T. Motobayashi, T. Nakabayashi, S. Nakajima, T. Nakamura, T. Ohtsubo, H. Sakurai, R. Shinoda, M. Shinohara, H. Suzuki, T. Suzuki, M. Takechi, E. Takeshita, S. Takeuchi, Y. Togano, K. Yamada, T. Yamaguchi, T. Yasuno, and M. Yoshitake, One- and two-neutron removal reactions from ^{19,20}C with a proton target, Phys. Rev. C **84**, 064315 (2011).

The publications listed here are those released in the fiscal year 2011 by all the workers listed on p.39.

5. M. Takechi, T. Ohtsubo, M. Fukuda, D. Nishimura, T. Kuboki, T. Suzuki, T. Yamaguchi, A. Ozawa, T. Moriguchi, H. Ooishi, D. Nagae, H. Suzuki, S. Suzuki, T. Izumikawa, T. Sumikama, M. Ishihara, H. Geissel, N. Aoi, Rui-Jiu Chen, De-Qing Fang, N. Fukuda, I. Hachiuma, N. Inabe, Y. Ishibashi, Y. Ito, D. Kameda, T. Kubo, K. Kusaka, M. Lantz, Yu-Gang Ma, K. Matsuta, M. Mihara, Y. Miyashita, S. Momota, K. Namihira, M. Nagashima, Y. Ohkuma, T. Ohnishi, M. Ohtake, K. Ogawa, H. Sakurai, Y. Shimbara, T. Suda, H. Takeda, S. Takeuchi, K. Tanaka, R. Watanabe, M. Winkler, Y. Yanagisawa, Y. Yasuda, K. Yoshinaga, A. Yoshida, K. Yoshida, Interaction cross sections for Ne isotopes towards the island of inversion and halo structures of ^{29}Ne and ^{31}Ne, Physics Letters B **707,** 357-361 (2012).

MATERIALS AND CLUSTER SCIENCE

6. Takuro Yoshikawa, Yasushi Kanke, Hideto Yanagihara, Eiji Kita, Yorihiko Tsunoda, Kiiti Siratori, Kay Kohn, Mössbauer study on the antiferromagnetic FeO synthesized under high pressure, Hyperfine Interact., 205 (2012)135-138

7. Hideto Yanagihara, K. Uwabo, Makoto Minagawa, Eiji Kita, and Nobuyuki Horita, Perpendicular magnetic anisotropy in $CoFe_2O_4$(001) films epitaxially grown on MgO(001), J. Appl. Phys., 109 (2011) 07C122

8. Masataka Ohkubo, Shigetomo Shiki, Masahiro Ukibe, Shigeo Tomita, Shigeo Hayakawa, “Direct mass analysis of neutral molecules by superconductivity”, Int. J. Mass Spectrom. 299, 94-101, (2011)

9. K. Harada, K. S. Makabe, H. Akinaga, and T. Suemasu, “Room temperature magnetoresistance in $Fe_3Si/CaF_2/Fe_3Si$ MTJ epitaxially grown on Si(111)”, J. Phys. Conference Series 266 , 012088 (2011) (5 pages).

10. K. Harada, K. S. Makabe, H. Akinaga, and T. Suemasu, “Magnetoresistance characteristics of $Fe_3Si/CaF_2/Fe_3Si$ heterostructures grown on Si(111) by molecular beam epitaxy”, Physics Procedia 11, 15-18 (2011).

11. S. Yin, M. Takahashi, R. Miida, H. Iwasaki and Ken-ichi Ohshima, “X-ray Diffraction Study of the Ordered Structures and Phase Relation in Pd-Mn Alloy System”, Materials Transactions **52**, 374 - 379 (2011).

12. A. Uedono, S. Ishibashi, K. Tenjinbayashi, T. Tsutsui, K. Nakahara, D. Takamizu, and S. F. Chichibu, “Defect characterization in Mg-doped GaN studied using a monoenergetic positron beam,” J. Appl. Phys. 111, 014508(1-6) (2012).

13. A. Uedono, K. Tenjinbayashi, T. Tsutsui, Y. Shimahara, H. Miyake, K. Hiramatsu, N. Oshima, R. Suzuki, and S. Ishibashi, “Native cation vacancies in Si-doped AlGaN studied by monoenergetic positron beams,” J. Appl. Phys. 111, 013512(1-5) (2012).

14. M. Sometani, R. Hasunuma, M. Ogino, H. Kuribayashi, Y. Sugahara, A. Uedono, and K. Yamabe, “Variation of chemical vapor deposited SiO2 density due to generation and shrinkage of open space during thermal annealing,” Jpn. J. Appl. Phys. 51, 021101(1-3) (2012).

15. A. S. Hamid, A. Uedono, Zs. Major, T. D. Haynes, J. Laverock, M. A. Alam, and S. B. Dugdale, D. Fort, “Electronic structure and Fermi surface of the weak ferromagnet Ni_3Al,” Phys. Rev. B 84, 235107 (2011).

16. Y. Oka, A. Uedono, K. Goto, Y. Hirose, M. Matsuura, M. Fujisawa, and K. Asai, “Structure-modification model of progen-based porous SiOC film with ultraviolet curing,” Jpn. J. Appl. Phys. 50, 05EB06(1-5) (2011).

17. S. F. Chichibu, K. Hazu, T. Onuma, and A. Uedono, “Collateral evidence for an excellent radiative performance of $Al_xGa_{1-x}N$ alloy films of high AlN fractions,” Appl. Phys. Lett. **99**, 051902(1-3) (2011).

18. M. M. Islam, A. Uedono, S. Ishibashi, K. Tenjinbayashi, T. Sakurai, A. Yamada, S. Ishizuka, K. Matsubara, S. Niki, and K. Akimoto, “Impact of Cu/III ratio on the near-surface defects in polycrystalline $CuGaSe_2$ thin films,” Appl. Phys. Lett. **98**, 112105(1-3) (2011).

19. N. Oshima, B. E. O’Rourke, R. Kuroda, R. Suzuki, H. Watanabe, S. Kubota, K. Tenjinbayashi, A. Uedono, and N. Hayashizaki, “Slow positron beam apparatus for surface and subsurface analysis of samples in air,” Appl. Phys. Express **4**, 066701(1-3) (2011).

20. E. Mume, D. E. Lynch, A. Uedono, S. V. Smith, “Investigating the binding properties of porous drug delivery systems using nuclear sensors (radiotracers) and positron annihilation lifetime spectroscopy-Predicting conditions for optimum performance,” Dalton Transactions **40**, 6278-6288 (2011).

21. A. Uedono, S. Ishibashi, S.F. Chichibu and K. Akimoto, “Point defects in GaN and related group-III nitrides studied by means of positron annihilation,” Gallium Nitride Materials and Devices VI, edited by J.-I. Chyi, Y. Nanishi, H. Morkoç, J. Piprek, E. Yoon, Proc. of SPIE Vol. 7939, 79390I(1-10) (2011).

22. E. Mume, A. Uedono, G. Mizunaga, D. E. Lynch, and S. V. Smith, “The role of positron annihilation lifetime studies and nuclear sensors for characterizing porous materials,” 12th International Workshop on Slow Positron Beam Techniques (SLOPOS12), Journal of Physics: Conference Series **262**, 012040(1-4) (2011).

23. N. Oshima, R. Suzuki, T. Ohdaira, A. Kinomura, S. Kubota, H. Watanabe, K. Tenjinbayashi, A. Uedono, and M. Fujinami, “Imaging of the distribution of average positron lifetimes by using a positron probe microanalyzer,” 12th International Workshop on Slow Positron Beam Techniques (SLOPOS12), Journal of Physics: Conference Series **262**, 012044(1-4) (2011).

24. S. Sellaiyan, S. V. Smith, A. E. Hughes, A. Miller, D. R. Jenkins, and A. Uedono, “Understanding the effect of nanoporosity on optimizing the performance of self-healing materials for anti-corrosion applications,” 12th International Workshop on Slow Positron Beam Techniques (SLOPOS12), Journal of Physics: Conference Series **262**, 012054(1-4) (2011).

25. A. Uedono, S. Ishibashi, N. Oshima, T. Ohdaira, and R. Suzuki, “Application of positron annihilation technique to front and backend processes for modern LSI devices,” 12th International Workshop on Slow Positron Beam Techniques (SLOPOS12), Journal of Physics: Conference Series **262**, 012061(1-4) (2011).

26. A. Uedono, S. Ishibashi, S. F. Chichibu, and K. Akimoto, “Point defects in GaN and related group-III nitrides studied by means of positron annihilation,” Gallium Nitride Materials and Devices VI, ed. J.-I. Chyi, Y. Nanishi, H. Morkoc, and J. Piprek, E. Yoon, Proc. of SPIE **7939**, 79390I (1-10) (2011).

27. E. Mume, A. Uedono, G. Mizunaga, D. L. Lynch, and S. V. Smith, “The role of positron annihilation lifetime studies and nuclear sensors for characterizing porous materials,” J. Phys.: Conf. Ser. **262**, 012040(1-4) (2011).

28. N. Oshima, R. Suzuki, T. Ohdaira, A. Kinomura, S. Kubota, H. Watanabe, K. Tenjinbayashi, A. Uedono, and M. Fujinami, “Imaging of the distribution of average positron lifetimes by using a positron probe microanalyzer,” J. Phys.: Conf. Ser. **262**, 012044(1-4) (2011).

29. S. Sellaiyan, S. V. Smith, A. E. Hughes, A. Miller, D. R. Jenkins, and A. Uedono, “Understanding the effect of nanoporosity on optimizing the performance of self-healing materials for anti-corrosion applications,” J. Phys.: Conf. Ser. **262**, 012054(1-4) (2011).

30. A. Uedono, S. Ishibashi, N. Oshima, T. Ohdaira, and R. Suzuki, “Application of positron annihilation technique to front and backend processes for modern LSI devices,” J. Phys.: Conf. Ser. **262**, 012061(1-4) (2011).

ACCELERATOR MASS SPECTROMETRY

31. S. Merchel, W. Bremser, V. Alfimov, M. Arnold1, G. Aumaître, L. Benedetti, D. L. Bourlès, M. Caffee, L. K. Fifield, R. C. Finkel, S. P. H. T. Freeman, M. Martschini, Y. Matsushi1, D. H. Rood, K. Sasa, P. Steier, T. Takahashi, M. Tamari, S. G. Tims, Y. Tosaki, K. M. Wilcken and S. Xu, Ultra-trace analysis of ^{36}Cl by accelerator mass spectrometry: an interlaboratory study, Analytical and Bioanalytical Chemistry, **400**, (2011), 3125-3132. doi:10.1007/s00216-011-4979-2.

32. Norikazu Kinoshita, Keisuke Sueki, Kimikazu Sasa, Jun-ichi Kitagawa, Satoshi Ikarashi, Tomohiro Nishimura, Ying-Shee Wong, Yukihiko Satou, Koji Handa, Tsutomu Takahashi, Masanori Sato, Takeyasu Yamagata, First assessment of individual radionuclides distributions from the Fukushima nuclear accident covering central-east Japan, Proceedings of the National Academy of Sciences (PNAS), (2011). doi:10.1073/pnas.1111724108.

33. Yuki Tosaki, Norio Tase, Kimikazu Sasa, Tsutomu Takahashi, Yasuo Nagashima, Measurement of ^{36}Cl deposition flux in central Japan: Natural background level and its seasonal variability, Journal of Environmental Radioactivity, Journal of environmental radioactivity, **106,** 73-80 (2012).

34. N. Kinoshita, M. Paul, Y. Kashiv, P. Collon, C. M. Deibel, B. DiGiovine, J. P. Greene, D. J. Henderson, C. L. Jiang, S. T. Marley, T. Nakanishi, R. C. Pardo, K. E. Rehm, D. Robertson, R. Scott, C. Schmitt, X. D. Tang, R. Vondrasek, A. Yokoyama, A Shorter ^{146}Sm Half-Life Measured and Implications for ^{146}Sm-^{142}Nd Chronology in the Solar System, Science, **30** March (2012), Vol. 335 no. 6076 pp. 1614-1617.

INTERDISCIPLINARY RESEARCH

35. K. Nomura, Y. Ohki, M. Fujimaki, X. Wang, K. Awazu, T. Komatsubara, A study of the critical factor determining the size of etched latent tracks formed on SiO_2 glass by swift-Cl-ion irradiation, Nuclear Instruments and Methods in Physical Research B **272,** 1-4 (2012).

5.2 International conferences

1. Akira Ozawa, 'Overview of Rare-RI Ring and mass measurements', RIBF-ULIC-Symposium-009 'Physics of Rare-RI Ring', Nov. 10-12, (2011), Wako, RIKEN Nishina Center, Japan, **(Invited talk)**

2. Daisuke Nagae, 'TOF detector for RIKEN Rare-RI Ring', RIBF-ULIC-Symposium-009 'Physics of Rare-RI Ring', Nov. 10-12, (2011), Wako, RIKEN Nishina Center, Japan, **(Invited talk)**

3. Yuki Tosaki, Norio Tase, Kimikazu Sasa, Tsutomu Takahash and Yasuo Nagashima, Estimation of Groundwater Age Using the ^{36}Cl Bomb Pulse: a Case Study in the Mt. Fuji Area, Central Japan, AOGS 2011, Aug. 08-12 (2011). **(Invited talk)**

4. A. Uedono, S. Ishibashi, N. Oshima, T. Ohdaira, and R. Suzuki, "Defects in GaN and group-III nitrides studied by positron annihilation technique," The international Workshop on Positron Studies of Defects 2011, Delft University of Technology, Delft, Netherlands, 28 August, (2011). **(Invited talk)**

5. A. Uedono, **"** Detection of point defects in semiconductor device materials by monoenergetic positron beams **"**, IMEC Kapeldreef 75, B-3001 Leuven, Belgium, 2 Sept., (2011). **(Invited talk)**

6. A. Uedono, **"** Characterization of semiconductor device materials by means of positron annihilation technique **"**, Australian Nuclear Science and Technology Organization (ANSTO), Bragg Institute Seminar, Kirrawee DC NSW 2232, Australia, 21 July, (2011). **(Invited talk)**

7. Peter Schury, 'MRTOF at RIKEN', RIBF-ULIC-Symposium-009 'Physics of Rare-RI Ring', Nov. 10-12, (2011), Wako, RIKEN Nishina Center, Japan

8. Takuro Yoshikawa, Yasushi Kanke, Hideto Yanagihara, Eiji Kita, Yorihiko Tsunoda, Kiiti Siratori, Kay Kohn, "Mössbauer study on the antiferromagnetic FeO synthesized under high pressure", International Conference on the Applications of the Mössbauer Effect, 25-30 September 2011, Kobe

9. K. Sasa, S. Ishii, and M. Kurosawa, Micro-PIXE system for geosciences applications at the Tsukuba 1 MV Tandetron accelerator facility, the 7th International Symposium on Bio-PIXE (BioPIXE7), Tohoku University, Sendai, Japan, 30 Oct. - 4 Nov. (2011).

10. Kimikazu Sasa, Tsutomu Takahashi and Keisuke Sueki, New AMS project at the University of Tsukuba, The 4th East Asia AMS Symposium, 16-18 December, (2011), Takeda Hall, The University of Tokyo.

11. Yuki Matsushi, Kimikazu Sasa, Kazuna Kurosumi, Tsutomu Takahashi, Kazuho Horiuchi, Yuki Tosaki, Keisuke Sueki, Hiroyuki Matsuzaki, Motohiro Hirabayashi and Hideaki Motoyama, Long-term ^{36}Cl depositional flux recorded in the Dome Fuji ice core, Antarctica: a possible link to climate change in mid latitudes during the last two deglaciations, The 4th East Asia AMS Symposium, 16-18 December, (2011), Takeda Hall, The University of Tokyo.

12. Keisuke Sueki, Jun-ichi Kitagawa, Takahiro Amano, Michiko Tamari, Kimikazu Sasa, Tsutomu Takahashi, Norikazu Kinoshita, Hangtao Shen, Yuki Tosakii, Yuki Matsushi and Matuzaki Distributions of radionuclides ^{36}Cl and ^{129}I in surface soils, The 4th East Asia AMS Symposium, 16-18 December, (2011), Takeda Hall, The University of Tokyo.

13. Yuki Tosaki, Norio Tase, Kimikazu Sasa, Tsutomu Takahashi, Sonia Gmati and Sayako Ueno, Characterization of groundwater chemistry and ages in volcanic aquifers of the southern foot of Mt. Fuji, central Japan, The 4th East Asia AMS Symposium, 16-18 December, (2011), Takeda Hall, The University of Tokyo.

14. Shigeo Tomita, "Correlation between consumption of SO_2 and Nucleation Rate in $N_2/H_2O/SO_2$ by Irradiation of 20 MeV protons", The 2nd Nagoya Workshop on the Relationship between Solar Activity and Climate Changes, Jan. 16-17, (2012), Nagoya, Japan

15. M. Takahashi, H. Kato, K. Ohshima, Y. Noda, T. Shishido, "Atomic order and Magnetism in $Pt_{1-x}Mn_x$(x = 0.11 ~ 0.14) ", 1st Asia-Oceania Conference on Neutron Scattering (1st AOCNS), Nov. 20-24, (2011), Tsukuba EPOCAL, Tsukuba, Japan

16. K. Harada, Room temperature magnetoresistance in $Fe_3Si/CaF_2/Fe_3Si$ MTJ epitaxially grown on Si(111), 2nd International Symposium on Advanced Magnetic Materials and Applications, July 12-16, (2010), Sendai, Japan

17. K. Harada, Magnetoresistance characteristics of $Fe_3Si/CaF_2/Fe_3Si$ heterostructures grown on Si(111) by molecular beam epitaxy, APAC-Silicide 2010, July 24-26, (2010), Tsukuba EPOCAL, Tsukuba, Japan

6. THESES

Ph. D. theses

Tetsuaki MORIGUCHI	Density distributions for two neutron halo nuclei ^{8} Li and ^{14}Be deduced by the reaction cross section measurements
Suguru SATO	Analysis of coercive force mechanisms in soft and hard magnetic nano-materials

Master's theses

Yasushi ABE	Developments of time-of-flight detector for RI beams using secondary electron emission from carbon foil
Kimitake OKUMURA	Measurements of production cross sections for Al isotopes from ^{48}Ca beam
Shota FUKUOKA	Developments of lumped parameter type kicker magnet with impedance matching for J-PARC main ring
Sosuke NAKAMURA	Developments high efficiency ESI using RF carpet for mass calibration
Hideomi TANIKAWA	Correlation between Droplet Yield and the Consumption of SO_2 in the Nuclation process by Irradiation of 20MeV protons in $N_2/H_2O/SO_2$
Shinya TAMURA	Measurements of secondary electrons emitted by C_n^+ using MCP
Kazunori HARADA	Investigation of density of states of Fe_3Si and fabrication of magnetic tunnel junction devices
Kazuna KUROSUMI	Analysis of cosmogenic ^{36}Cl from the last deglaciation to Holocene in the Dome Fuji ice core , Antarctica.
Keisuke ODA	Growth of rare earth doped Gallium Nitride and its characterization
Keisuke KURITA	Development of photoemission spectroscopy apparatus for electronic structure investigation of H/Pd(110)
Yohei NARITA	Hydrogen uptake process into Mg multilayer observed by nuclear reaction analysis

Undergraduate theses

Syunsuke OKADA	Design of septum magnet of Rare-RI Ring
Yuta SAITO	Beam-optics for injection line in Rare-RI Ring
Momo MUKAI	DSMC simulation of rarefied gas flow inside Cluster-I]
Takahiro ONISHI	Study of nucleosynthesis by means of scandium 45 + proton reaction
Yoko SHIINA	Coincidence measurements between transmitted ions and secondary electron yields
Isao HARAYAMA	Correlation between Droplet Yield and the Consumption of SO_2 in the Nucleation process by corona discharge in $N_2/H_2O/SO_2$
Katsuya YAMAZAKI	Developmet of TOF Mass Spectrometer
Kenta CHITO	Development of high-resolution RBS for observation of graphite intercaration
Shunya HARADA	Development of ambient-NRA for observation of hydrogen uptake process into Mg thin film

7. SEMINARS

2011

April 15 Comparison of elliptic flow among various Identified hadrons and understanding of radial and elliptic expansion in 200GeV Au+Au at RHIC-PHENIX, *Yoshimasa Ikeda (University of Tsukuba)*

2012

Jan 23 Development of time-of-flight detector for RI-beam utilizing secondary electron emission from carbon foil, *Yasushi Abe (University of Tsukuba)*

Measurements of production cross-section for Al isotopes by a ^{48}Ca beam, *Kimitake Okumura (University of Tsukuba)*

Study of the multiplicity dependence of the jet energy balance in p+p collisions at $\sqrt{s}$ = 7 TeV by the LHC-ALICE experiment, *Shintaro Kubota (University of Tsukuba)*

Jan 26 Study of multi-particle correlations in Pb+Pb collisions at $\sqrt{s_{NN}}$ = 2.76TeV by the LHC-ALICE experiment, *Yuki Kondo (University of Tsukuba)*

Study of Higher Harmonic Azimuthal anisotropy in Pb+Pb collisions at $\sqrt{s_{NN}}$ = 2.76TeV by the LHC-ALICE experiment, *Hitoshi Nakazato (University of Tsukuba)*

Development of an efficient ESI using RF carpet for mass calibration, *Sosuke Nakamura (University of Tsukuba)*

Jan 30 Study of identified particle higher harmonic azimuthal anisotropyin Au+Au collisions at $\sqrt{s_{NN}}$ = 200GeV by the RHIC-PHENIX experiment, *Sanshiro Mizuno (University of Tsukuba)*

Developments for impedance matching and lumped-constant kicker magnet in J-PARC Main Ring, *Shota Fukuoka (University of Tsukuba)*

March 7 A new measurement of the astrophysical ^{8}Li(α,n)^{11}B reaction with the GEM-MSTPC, *Kanako Yamaguchi (University of Tsukuba)*

8. SYMPOSIUM

=== A debrief meeting of the Pre-Strategic Initiatives ===
A new dimension of the multi-tandem accelerator facility
at the University of Tsukuba
29 March 2012
Laboratory of Advanced Research B 0110

1. **Openning : *E. Kita (University of Tsukuba)***

2. Disaster situation of the multi-tandem accelerator facility at the University of Tsukuba and overview of the update scheme for the new tandem accelerator : *K. Sasa (University of Tsukuba)*

3. Studies of $^{12}C+^{4}He \rightarrow {}^{16}O+\gamma$ reaction and triple-nuclei-reaction-mechanics in Kyushu University : *K. Sagara (Kyushu University)*

4. Nucleosynthesis associated with $^{12}C(\alpha,\gamma)^{16}O$ reaction : *H.Makii (JAEA)*

5. Studies of magnetic moments with polarized unstable nuclei and its applications for material science : *K. Matsuta (Osaka University)*

6. Studies of Nucleosysthesis by using proton pulsed beam : *T. Hayakawa (JAEA)*

7. Nuclear astrophysics with 1MV Tandetron accelerator : *T. Komatsubara (University of Tsukuba)*

8. Overview of accelerator mass spectrometry with multi-nuclide : *H.Matsuzaki (The University of Tokyo)*

9. Archaeological studies for west Asian civilization – Anticipation for ^{14}C dating – : *A. Tsuneki (University of Tsukuba)*

10. Perspectives of accelerator mass spectrometry for geological science : *K.Horiuchi (Hirosaki University)*

11. New methodology of dating with accelerator mass spectroscopy : *H.Matsumura (KEK)*

12. Research activities of AMS study for environmental science in the University of Tsukuba : *K. Sueki (University of Tsukuba)*

13. Elemental analysis on surface and/or interface of materials by using high resolution RBS : *K. Kimura (Kyoto University)*

14. Industrial applications of nanoscale pore produced by heavy-ion-irradiation-technique : *M. Fujimaki (National Institute of Advanced Industrial Science and Technology (AIST))*

15. Industrial uses and ion-beam applications in RIBF at RIKEN : *T. Kanbara (RIKEN)*

16. PIXE analysis for geological science : *M. Kurosawa (University of Tsukuba)*

17. Electron excitation process induced by fast ion-cluster irradiation : *S. Tomita (University of Tsukuba)*

18. Device developments by use of electron-positron-annihilation γ–ray analysis : *A.Uedono (University of Tsukuba)*

19. Closing remarks: *A. Ozawa (University of Tsukuba)*

9. LIST OF PERSONNEL

Tandem Accelerator Complex

E. Kita	Director, Professor
K. Sasa	Associate Professor
T. Komatsubara	Assistant Professor
D. Sekiba	Assistant Professor
H. Kimura	Computer Engineer
H. Oshima	Electric Engineer
Y. Tajima	Mechanical Engineer
S. Ishii	Mechanical Engineer
T. Takahashi	Electric Engineer
Y. Yamato	Electric Engineer
N. Kinoshita	Research Fellow
Y. Tagishi	Research Supporter
K. Iitake	Administrative Stuff
N. Yamada	Administrative Stuff
S. Abe	Administrative Stuff

Research Members[1]

Inst. of Physics

I. Arai	T. Komatsubara	D. Nagae	A. Ozawa
K. Sasa	P. Schury		

Inst. of Applied Physics

K. Akimoto	S. Aoki	E. Kita	M. Minagawa
D. Sekiba	T. Suemasu	S. Tomita	A. Uedono
H. Yanagihara			

Inst. of Materials Science

T. Kondo	M. Takahashi

Inst. of Engineering Mechanics and Systems

K. Matsuuchi

[1]The "research members" include the authors and coauthors within 5 years back from this fiscal year, as well as the members of research projects running at UTTAC.

Inst. of Geoscience

M. Kurosawa

Inst. of Chemistry

K. Sueki

Staff of Open Advanced Facilities Initiative

H. Kudo	H. Naramoto	H. Shen	S. Yamazaki
M. Matsumura	H. Muromachi		

Graduate students

Doctoral Programs of Pure and Applied Science

Y. Ishibashi	K. Ito	Y. Ito	T. Moriguchi
S. Sato	K. Suzuki	K. Yamaguchi	

Master's Programs of Pure and Applied Science

Y. Abe	S. Fukuoka	S. Funada	D. Isaka
M. Iura	Y. Kiguchi	J. Kitagawa	K. Kurita
H. Mita	T. Mizunaga	S. Nakamura	Y. Narita
R. Nishikiori	T. Niwa	K. Oda	K. Okumura
N. Takemoto	S. Tamura	H. Tanikawa	K. Tenjinbayashi
T. Tsutsui	M. Uehira	Y. Yamashita	S. Yoshimatsu
T. Yuasa	Y. Watahiki		

Master's Programs of Life and Environmental Science

M. Ishikawa	K. Kurozumi	Y. Sato	Y. Wong

Undergraduates

K. Chito	S. Harada	I. Harayama	S. Kimura
A. Mori	M. Mukai	S. Okada	T. Onishi
Y. Saito	T. Sanai	S. Shohata	Y. Shiina
K. Yamazaki	T. Watanabe		

Scientific Gutests and Fellows

K. Awazu	National Institute of Advanced Industrial Science and Technology (AIST)
M. Fujimaki	National Institute of Advanced Industrial Science and Technology (AIST)
Y. Tosaki	National Institute of Advanced Industrial Science and Technology (AIST)
T. Hayakawa	Japan Atomic Energy Agency (JAEA)
T. Shizuma	Japan Atomic Energy Agency (JAEA)
S. Kubono	Center for Nuclear Study, Univ. of Tokyo (CNS)
A. Sato	Osaka Univ.
A. Yamamoto	High Energy Accelerator Research Organization (KEK)
T. Adachi	High Energy Accelerator Research Organization (KEK)
M. Yoshida	High Energy Accelerator Research Organization (KEK)
N. Kawamura	High Energy Accelerator Research Organization (KEK)
K. Shimomura	High Energy Accelerator Research Organization (KEK)
P. Strasser	High Energy Accelerator Research Organization (KEK)
T. Nakamoto	High Energy Accelerator Research Organization (KEK)
M. Iio	High Energy Accelerator Research Organization (KEK)
K. Yoshimura	High Energy Accelerator Research Organization (KEK)